Diss. ETH No. 28579

Capacitance and Tunnelling Studies on GaAs/AlGaAs based Electron-Hole Bilayers

A thesis submitted to attain the degree of
DOCTOR OF SCIENCES of ETH ZURICH
(Dr. sc. ETH Zurich)

presented by

Simon D. Parolo

Master of Science in Interdisciplinary Science (ETH Zurich)
born on 27.04.1990
citizen of Willisau (LU), Switzerland

accepted on the recommendation of

Prof. Dr. Werner Wegscheider, examiner
Prof. Dr. Oded Zilberberg, co-examiner

2022

Zusammenfassung

Diese Arbeit befasst sich mit Elektronen-Loch Doppellagen, welche räumlich nahe beieinander sind. Mit Hilfe eines MBE-Systems werden p-i-n Heterostrukturen gewachsen, in welchen die Doppellagen erzeugt werden. Die räumliche Trennung der Ladungen erfolgt über eine isolierende Barriere. Die Stärke der Wechselwirkung der 2D Ladungsschichten wird durch die Dicke der Barriere bestimmt. Es wird erwartet, dass bei hoher Wechselwirkung (i.e. dünne Barriere) Excitonen kreiert werden. Zusätzlich sagen Theorien vorher, dass diese Excitonen, bei genügend tiefen Temperaturen, den Zustand eines Bose-Einstein-Kondensats einnehmen können.

Der Einfluss der Barrierendicke auf das Verhalten des Doppellagen-Systems wird mittels Kapazitäts- und Leitfähigkeitsmessungen untersucht. Eine angelegte DC Spannung treibt die Ladungsträger aus den dotierten Schichten zur Barriere. Sobald sich die Elektronen- und Löcher-Systeme an der Barriere gebildet haben, kann eine Erhöhung der Kapazität beobachtet werden.

Experimente mit schwach interagierenden Elektronen-Loch-Systemen (i.e. eine Barrieren-Dicke von 20 nm) zeigen kein Tunneln von Ladungen oder Leckströmen, auch nicht bei hohen Spannungen. In Messungen mit einem angelegten Magnetfeld kann die Entstehung von Landau Levels beobachtet werden. Dies legt nahe, dass die Ladungssysteme einen 2D Charakter haben.

Eine Erhöhung der Wechselwirkung (i.e. Barrieren Dicke von 10 nm) zeigte keine Veränderung gegenüber der 20 nm dicken Barriere. Wird die dünnere Barriere jedoch mit einem Quantum Well (auf der p-dotierten Seite) kombiniert, verändert sich das Verhalten der Probe radikal. Mit dieser Anordnung konnten Oszillationen der Kapazität und Leitfähigkeit, als Funktion der angelegten Spannung, beobachtet werden. Diese Oszillationen überraschen durch ihre Regelmässigkeit und ihre Amplitude kann die geometrische Kapazität überragen.

Es wird gezeigt, dass dieses Verhalten mit resonantem Tunneln (RT) von Elektronen übereinstimmt und als Ursache der Oszillationen angenommen werden kann. Weiterführende Experimente zeigen, dass die Periode dieser Oszillationen mit dem Inversen der Dicke des Quantum Wells skaliert. Ebenfalls unterdrückt ein genügend grosses paralleles Magnetfeld die Oszillationen vollständig. Diese Resultate unterstützen das Bild des resonanten Tunnelns von Elektronen.

Ein weiterer Quantum Well auf n-dotierten Seite der Barriere beeinflusst die Oszillationen in keiner Weise. Dies führt zur Annahme, dass das Phänomen vielmehr durch das Tunneln von Elektronen zustande kommt und nicht durch das Tunneln von Löchern.

Es konnten keine RT-Oszillationen beobachtet werden, wenn die Wechselwirkung eine gemässigte Stärke hatte (i.e. eine 15 nm dicke Barriere). Jedoch wurden andere interessante Effekte gemessen, z.B. eine Hysterese im Spannungsverhalten oder das Auftreten einer atypischen Struktur in einem Landau Fan. Diese

Features passen nicht ins Bild des resonanten Tunnelns und bedürfen weiterer Forschung.

Diese Arbeit dient hoffentlich als Vorläufer für zukünftige Forschungen über Elektronen-Loch Doppellagen Systeme.

Abstract

This thesis studies two dimensional electron-hole bilayers in close spatial proximity. The charge layers are produced in an MBE grown p-i-n heterostructure and are separated by an insulating barrier. The width of the barrier determines the interaction strength between the two 2D layers. At high interaction strength (i.e. small barrier width), the formation of excitons is expected. In addition, theory predicts the Bose-Einstein condensation of the excitons at sufficiently low temperatures.

In order to study the effect of the barrier width on the device behaviour, capacitance and conductance measurements were performed. Here, an applied DC bias pushes the charges from the doping layers towards the barrier and a rise in capacitance can be observed as soon as the two charge systems form on each side of the barrier.

Experiments on weakly interacting charge systems (i.e. a barrier width of 20 nm) showed no tunnelling or leakage even at high bias voltages. Further measurements with a magnetic field showed the formation of Landau levels. This suggest that the charge layers have a 2D character.

An increase in the interaction strength (i.e. reducing the barrier width to 10 nm) did not change the observed behaviour. However, the reduced barrier width, combined with the introduction of a quantum well (QW) adjacent to the barrier on the p-doped side, led to a drastic change in device response. In this case, oscillations in capacitance and differential conductance as a function of bias voltage were observed. These oscillations are surprisingly regular, and their amplitude can exceed the geometric capacitance.

It is shown that this behaviour is consistent with resonant tunnelling (RT) of electrons being the origin of the oscillations. Further experiments have also shown that the oscillation period scales with the inverse of the QW width and that a sufficiently large parallel B-field suppresses the oscillations completely. This is in agreement with the resonant tunnelling picture.

Interestingly, adding a quantum well on the n-side of the barrier did not change the character of the oscillations. Therefore, it can be assumed that the phenomenon is caused by electron tunnelling rather than the tunnelling of holes.

An intermediate interaction strength (i.e. barrier width of 15 nm) did not show presence the of the RT-oscillations, but other interesting phenomena, e.g. hysteretic bias response or atypical features in a Landau fan. This does not align with the resonant tunnelling picture and needs to be investigated in future studies.

This work is hoped to be a precursor for further research on electron-hole bilayer systems in close spatial proximity.

Contents

Chapter 1

Introduction

The collective behaviour of charge carriers in solids has always intrigued physicists. Well-known examples are superconductivity or the fractional quantum Hall effect. These phenomena can be described using quasi-particles. In that picture transport and optical properties of electrons and holes can no longer be approximated by single particle behaviour anymore.

This thesis studies the behaviour of electrons and holes that are put in very close spatial proximity with the objective of finding and investigating novel and unusual phenomena. The interaction between the two types of charge carriers is investigated in the GaAs/AlGaAs semiconductor system. A standard semiconductor diode consisting of positively (p) and negatively (n) doped material is investigated in our experiments. Applying a positive voltage to the p-doping and a negative one to the n-doping pushes the charges towards a 10 nm thick barrier, where both an electron and a hole gas form with densities from zero up to more than $6 \times 10^{11} cm^{-2}$. The Coulomb interaction can lead to the formation of excitons with different properties than the two single 2D layers. Novel states like an exciton solid, either disordered or ordered as a Wigner crystal, can emerge. Even more intriguing would be the observation of an excitonic superfluid if the excitons undergo a Bose-Einstein condensation (BEC).

It turns out that a quantum well (QW) placed right at the barrier (separating the p- and n-doped regions) leads to novel and unusual capacitance and conductance oscillations. They originate from the long lifetime of electrons injected in high index energy levels of the QW, while holes occupy quantum states in the valence band. The resulting long recombination time is unexpected because, at first glance, the design is very similar to a light emitting diode (LED), where rapid electron-hole recombination under photon emission occurs.

This thesis was motivated by the possibility of improving previous experiments on the Bose-Einstein condensation in the GaAs/AlGaAs system by using the considerably higher purity semiconductor structures available at the ETH. It turned out that the used design, consisting of a thin barrier between electrons and holes, also gave access to entirely different phenomena, e.g. the tunnel injection of electrons into a quantum well.

The search for collective phenomena in the electron-hole system has a long history of theoretical and experimental investigations because of the possibility of finding a BEC. Early attempts to detect BEC in bulk semiconductors failed because the optically excited excitons recombined too fast [1, 2].

The exciton lifetimes could be increased by trapping the electrons and holes in spatially separated asymmetric quantum wells [3, 4] but the results remained unclear. Combining excitons with an optical resonator forms exciton-polaritons that indeed showed signatures of condensation [5, 6].

The coupling of the charges of an electron-hole bilayer to excitons in a semiconductor system had already been suggested in the previous century [7, 8]. Such devices have indeed been fabricated and measured and seemed to be a suitable candidate for exciton condensation [9, 10, 11, 12]. Alternatively, such a bilayer system can be fabricated using graphene sheets [13] separated by a barrier or from transition-metal dichalcogenides, such as $MoSe_2$ [14].

The semiconductor structures used in this thesis are based upon the earlier works done by M. Pohlt [10]. However, the designs were simplified by growing a p-i-n device with a barrier in the intrinsic region. Furthermore, the device capacitance rather than lateral transport is measured because it offers access to the density of states of the charge system.

There are indeed indications of possible exciton condensation at small densities in the milliKelvin regime. However, much more pronounced are the novel capacitance oscillations that are found if electrons are tunnel-injected into a quantum well already populated with holes.

Chapter 2 begins with a general introduction to semiconductor physics and is followed by discussions about excitons and capacitance. The behaviour of 2D systems in a magnetic field is also reviewed. The chapter closes with remarks on quantum tunnelling, focusing on resonant tunnelling.

Experimental methods are explained in **chapter 3**. First, molecular beam epitaxy is introduced, followed by a presentation of the heterostructures used in this work. The following section describes clean room processing and includes an introduction to the measurement methods.

Chapter 4 shows the experimental results measured on devices with low interaction strength between the electron and hole gas, also suggesting their 2D character.

Strong interaction within the bilayer systems was achieved by reducing the barrier width. In this regime, capacitance and conductance oscillations were observed. This novel phenomenon is described in **chapter 5** and it is shown that it can be attributed to resonant tunnelling [15].

Chapter 6 continues with results from systems with an intermediate interaction strength between the layers. In this regime, the capacitance oscillations vanish, but a hysteretic response to bias emerges. This behaviour cannot be explained by resonant tunnelling, and another model has to be developed in future research.

The last chapter summarises the results and gives an outlook on future research, **chapter 7**.

Chapter 2

Theory

A general introduction to semiconductor physics is presented in this chapter. The focus will be on the GaAs/AlGaAs system, which is used for the research of this thesis. An introduction of two dimensional (2D) charge systems and their behaviour in an external magnetic field follows. Double layer systems and the possibility of finding quasi-excitons from the inter-layer interactions will also be discussed. Capacitance and tunnelling will be introduced as the main methods to investigate the interlayer interactions. Particular attention will be directed to quantum capacitance and resonant tunnelling, respectively.

2.1 Semiconductor Basics

Electrical conductance can be used to classify materials. It is well known that current (electrons) can pass through a conductor (metal) with little resistance, whereas an insulator has a high resistance. A semiconductor is a solid body whose conductance is lower than that of metal but has a higher one compared to an insulator. In order to clarify this term, the band model of these three materials can be looked at, shown in figure 2.1. In this model, a solid body can be described by energy bands. It can be distinguished between allowed and forbidden energy zones, called energy bands and energy gaps. Electrons may only fill energy bands since there they find empty states. In the forbidden zones or gaps, no states are available to the electrons. In other words, the density of states (DOS) is zero. The bands are filled up to the Fermi energy E_F, which denotes the energy of the highest occupied electron level, at $T = 0\,\mathrm{K}$. The highest completely filled energy band is called the valence band E_V, and the one above it is the conduction band E_C. In the semiconductor and insulator (figure 2.1), E_F lies between the conduction and valence band, resulting in a completely filled valence band and an empty conduction band. Intuitively, an empty band does not contribute to electrical conductance since no charge carriers are present. However, charge carriers are present in the valence band, yet they do not conduct. In order to be conductive, electrons also need an empty state to move into. Since the valence band is completely filled, i.e. it has no empty states, electrons cannot move, and therefore no current is flowing. This leads to the conclusion that semiconductors and insulators do not conduct at $T = 0\,\mathrm{K}$. Figure 2.1 shows that the Fermi energy in a conductor is located within the conduction band. Therefore, occupied and empty states are available to the charge carriers with negligible energy spacing. This allows the conductor to be conductive most of the time. In order to differentiate between semiconductors and insulators, the energy gap between valence and conduction band (known as band gap) is used. Semiconductors have a smaller band gap than insulators usually ranging from $E_{\text{gap}} = 0.2\,\mathrm{eV}$ up to $3.4\,\mathrm{eV}$.

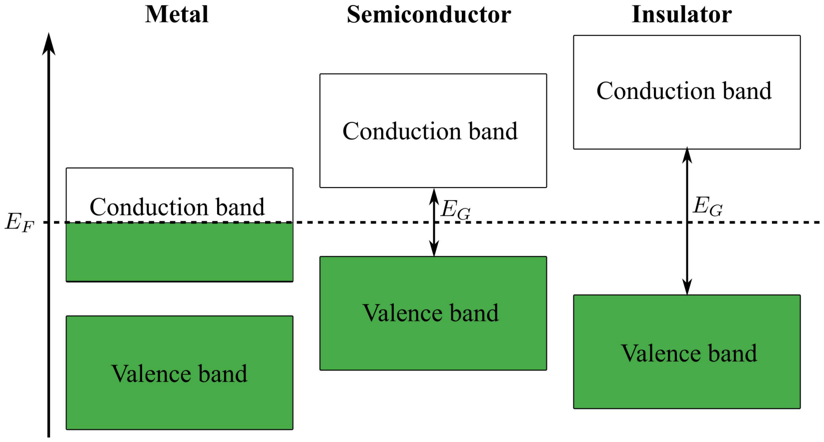

Figure 2.1: Schematic illustration of the conduction and valence band for a conductor (metal), a semiconductor and an insulator. The coloured region depicts the filling level of each band. Figure from [16].

2.1.1 The GaAs/AlAs Material System

Gallium arsenide (GaAs) is a III-V semiconductor. As the name already implies, it is a binary compound of the group III element gallium and the group V element arsenic. Gallium arsenide crystals form a face-centred cubic (fcc) lattice in a zincblende structure. Therefore, each gallium atom is neighboured by four arsenic atoms and vice versa. The lattice constant of GaAs is $a_0 = 5.653\,\text{Å}$. Figure 2.2 shows a schematic of the band structure of GaAs. It can be seen that the minimum of the conduction band and the maximum of the valence band are both at the Γ point. This characteristic is also known as a direct band gap. The gap energy of GaAs is $E_{\text{gap}} = 1.43\,\mathrm{eV}$ at $300\,\mathrm{K}$ and increases with lower temperature to $1.52\,\mathrm{eV}$ at $0\,\mathrm{K}$ [17]. Additionally, one sees that the valence band consists of three different bands, the heavy and light holes, as well as the split off band. Around the Γ point, the electron dispersion relation $E(\vec{k})$ can be described by the parabolic relation,

$$E(\vec{k}) \approx E_0 + \frac{\hbar^2 \vec{k}^2}{2m^*} \tag{2.1}$$

where m^* is the effective mass, $\vec{k}$ the wave vector and E_0 a constant [18]. Within this approximation, the effective mass is inversely proportional to the curvature of the band.

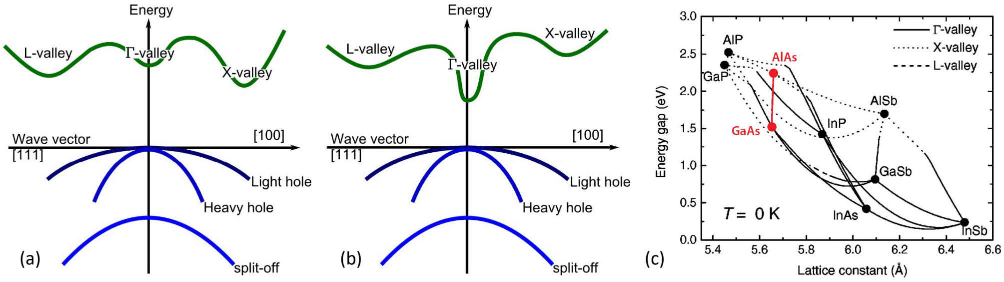

Figure 2.2: Schematic illustration of the band structure of (a) GaAs and (b) AlAs (figures taken from [19]). (c) Band gap energy as a function of the lattice constant for different semiconductor materials. Figure taken from [17].

Aluminium arsenide (AlAs) is also a III-V semiconductor which crystallises in a zincblende structure. Its lattice constant is $a_0 = 5.661$ Å, which is very close to the one of GaAs. Its schematic band structure is shown in figure 2.2. It can be seen that the minimum of the conduction band is not at the Γ point anymore (as in GaAs), but it has its minima at the X-valley. This results in AlAs being an indirect semiconductor with a gap energy of 2.28 eV at low temperature (for the indirect gap).

Due to the same crystal structure and similar lattice constant, GaAs and AlAs can be combined without any major drawbacks. This results in the ternary semiconductor $\mathrm{Al_xGa_{1\text{-}x}As}$. Here a fraction x of the gallium atoms is replaced with aluminium atoms. Figure 2.2 shows the band gap energy as a function of the lattice constant for different semiconductors, including the GaAs-AlAs system. The gap energy of $\mathrm{Al_xGa_{1\text{-}x}As}$ depends on the fraction of aluminium x. For a fraction smaller than 42% ($x < 0.42$) $\mathrm{Al_xGa_{1\text{-}x}As}$ has a direct band gap which changes to an indirect gap above this value.

The similar lattice constant and the different gap energies make the GaAs/AlAs system a good candidate for band structure engineering. Regions with different energy gaps can be grown rather easily on top of each other. That can be used to create heterostructures consisting of conducting channels and (tunnelling) barriers.

2.1.2 Two Dimensional Electron System

As already mentioned, the similar lattice constant of GaAs and AlAs (including $Al_xGa_{1-x}As$) allows an almost unstrained growth of the materials on top of each other. This is crucial for the phenomenon discussed here, the formation of a two dimensional electron gas (2DEG). The most basic way to create such a 2DEG is to combine two semiconductors with different gap energies forming a so-called heterojunction, GaAs and AlGaAs, for example. In order to adjust the different Fermi levels, the electrons provided to the structure move to the interface, where they deform the band structure of the heterojunction. This results in the conduction band being drawn below the Fermi level ($E_C < E_F$), creating a spatially confined region in which the electrons reside. Within this layer, they can move with meagre resistance, depending on the material quality.

The electrons can already be provided during the growth of the structure. This can be done by introducing doping atoms (yellow line in figure 2.3) during the growth. In the GaAs/AlAs system, silicon usually serves as a donor, providing electrons to the system, which move to the heterojunction and create the 2DEG. Such a structure can be seen in figure 2.3.

In order to increase the quality of the 2DEG, plenty of research has been carried out. One of the main factors limiting the quality is the scattering of the electrons. Since the doping atoms act as impurities, of which the electrons scatter, they are moved away from the 2DEG region. To increase the control of the distance between doping and heterojunction, all doping atoms are squeezed into a single δ-doping layer. The density of the resulting 2DEG can now be tuned by changing the two parameters, the doping density of the δ-doping and the distance between doping and 2DEG.

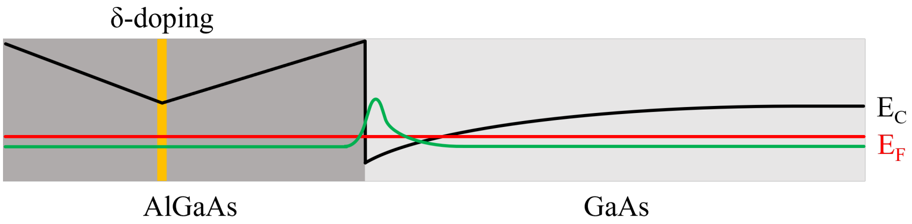

Figure 2.3: Schematic of the conduction band of a heterojunction with a delta doping away from the interface (yellow line). It can be seen, that at the interface the conduction band (black line) is drawn below the Fermi level (red line) and that in this region the electron density (green line) is at its maximum, forming the 2DEG.

Due to the doping, the 2DEG forms with a specific density (depending on the doping concentration and other growth factors). By adding a top or back gate to the structure, the density of the 2DEG can be tuned. A positive gate voltage increases the electron density in the 2DEG, whereas a negative voltage depletes it.

The same mechanisms can be used to manipulate the valence band. Holes, which are provided to the structure (usually done by carbon doping), travel to the GaAs/AlGaAs interface. This results, as with electrons, in a bending of the band structure. But opposite to the electrons ($E_C < E_F$), the valence band is now raised above the Fermi level, $E_V > E_F$, which leads to the formation of a two dimensional hole gas (2DHG). A metal gate can again be used to tune the density of the 2DHG but with reversed effect concerning polarity.

2.1.3 Quantum Wells

These two dimensional charge systems can be generated in various structures, such as the single quantum well (QW). It can be realised by sandwiching a low band gap material (e.g. GaAs) between semiconductors with larger gap energy (e.g. AlGaAs). This results in a square-shaped potential well, which confines the charges. Due to this confinement, the electrons can only occupy certain energy levels (subbands) within the QW. A schematic of such an undoped quantum well structure is shown in figure 2.4. The energy of these subbands can be determined by solving the Schrödigner equation. The subband energies of bound states can be approximated with the model of a quantum well with infinite potential barriers:

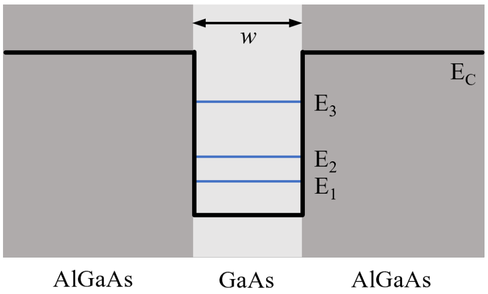

Figure 2.4: Schematic of an undoped single quantum well structure with well width w. For simplification only the conduction band and three discrete electron levels are drawn.

$$E_n = \frac{\pi^2 \hbar^2 n^2}{2m^* w^2} \tag{2.2}$$

where $n = 0, 1, 2, ...$ is the subband index and w the width of the quantum well and m^* the effective mass of the particle in the well [20]. One can see that the width of the well influences the spacing between the discrete energy levels. This is an important point for this thesis, to which is shown in section 5.3.3.

The last quantum structure presented here is the double quantum well (DQW). As the name already implies, it consists of two single quantum wells separated by a barrier. Figure 2.5 shows the semiconductor heterostructure and the energy bands of a DQW. In the case of a thin barrier, the subbands can interact with each other, forcing one to higher energy (anti-binding state) and the other to lower energy (binding state), figure 2.5(a). In the DQW system, it is possible to adjust the interaction strength between the two potential wells. Calculations show that at a barrier width of $d \geq 10\,\text{nm}$ the interaction strength is very small, and the double quantum well system can be treated as two individual single quantum wells [20], as shown in figure 2.5(b).

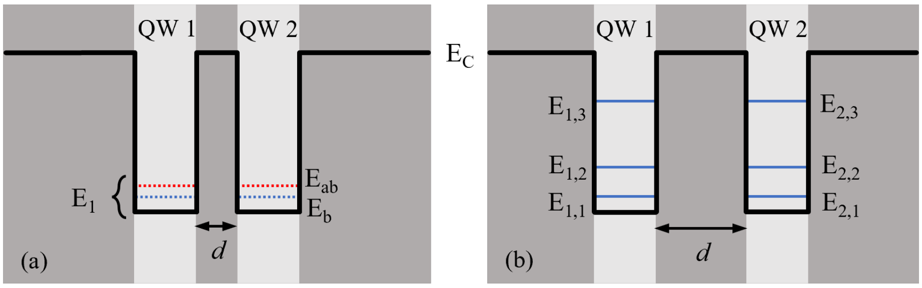

$d < 10$nm $\qquad$ $d \geq 10$nm

Figure 2.5: Schematic of an undoped double quantum well structure with barrier width d. For simplification, only the conduction band and three discrete electron levels are drawn. (a) for small d: splitting of the subbands into binding (blue dotted line) and anti-binding (red dotted line) levels. Only the lowest level is shown. (b) for large d: the interaction strength is small, therefore the double well system can be treated as two single wells.

2.2 Direct and Indirect Excitons

The exciton is a charge-neutral quasi-particle consisting of a bound electron-hole pair. Excitons can be generated in semiconductors, e.g. by optical excitation. An electron in the valence band absorbs an incident photon, which has an energy comparable to the band gap of the semiconductor. This excites the electron to the conduction band, leaving an empty state in the valence band, a so-called hole behind. Due to their attractive force, the electron and hole often enter a bound state, creating the exciton, figure 2.6(a). Due to the high effective mass of the hole, this two body system is similar to a hydrogen atom. The binding energy of the bulk exciton can be calculated:

$$E_{X^0}^{\mathrm{3D}} = -\frac{\mu e^4}{32\pi^2\hbar^2\epsilon_r^2\epsilon_0^2} \tag{2.3}$$

where ϵ_r is the relative permittivity, ϵ_0 the dielectric constant and μ the reduced mass of the exciton [20, 21]. For the electron-hole pair μ is given by

$$\frac{1}{\mu} = \frac{1}{m_e^*} + \frac{1}{m_h^*} \tag{2.4}$$

For Γ-valley electrons and holes in GaAs this results in a binding energy of $E_{X^0} = -4.7\,\mathrm{meV}$ which is in good agreement with experimental observations [22]. Although this binding energy is small, the bulk excitons can have lifetimes ranging from hundreds of picoseconds up to nanoseconds.

So-called dark excitons have even longer radiative lifetimes. Here, the recombination of electrons and holes can not occur via the emission of a photon due to spin conservation [23].

For spatially confined excitons (e.g. trapped in a quantum well, figure 2.6(b)), the confinement leads to a modification of the binding energy $E^{2D}_{X^0}$. Theoretically $E^{2D}_{X^0}$ can be four times larger than the one in bulk material, $E^{2D}_{X^0} = 4E^{3D}_{X^0}$ [20].

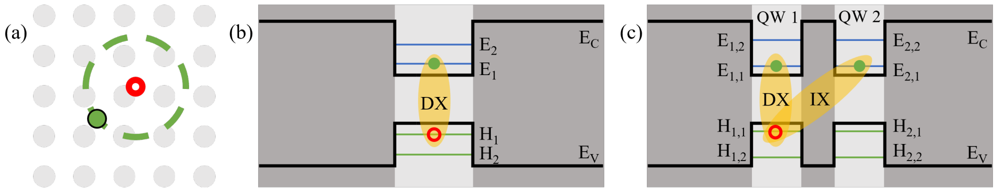

Figure 2.6: Schematic of a: (a) bulk exciton, the electron (green dashed ring) orbits around a hole (red dot), (b) exciton confined in a single quantum well. Since there is no spatial separation, it is a direct exciton. (c) excitons in a double quantum well. If the electron and hole reside in the same well, the resulting exciton is a direct (DX), whereas if they are spatially separated (different wells for electron and hole), an indirect exciton (IX) is created.

Within a double quantum well system, two kinds of excitons can form. If both electron and hole reside in the same quantum well, they form a direct exciton (DX). If they are spatially separated, i.e. they reside in different wells, the resulting quasi-particle is an indirect exciton (IX), see figure 2.6(c). Even though they are the same quasi-particle, direct and indirect excitons have different properties. Due to the spatial separation of the electron-hole pair, the IX has a dipole moment. Furthermore, experiments have shown that the indirect exciton has a longer lifetime than the direct one [24, 25]. Together with the bosonic nature of the exciton, this allows them to be cooled down, and they might form a Bose-Einstein-Condensate (BEC), which has been predicted by theory since the early 1960s [1].

2.3 Introduction to Capacitance

The capacitance C is a measure which indicates how much charge Q a capacitor can store at a certain potential difference $C = \frac{Q}{V}$. It is also associated with storing electrical energy $E = \frac{1}{2}CV^2$. One of the simplest versions of a capacitor is the plate capacitor. It consists, as the name already suggests, of two parallel conducting plates separated by a dielectric. The capacitance for such a plate capacitor is defined by its geometry as

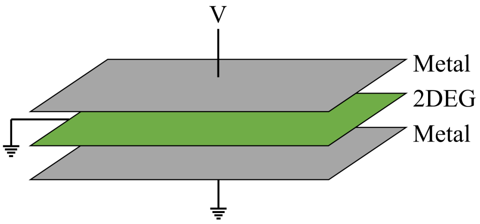

Figure 2.7: Schematic of a 2DEG (green layer) which is enclosed by two metal plates (gray layers). The lower metal layer and the 2DEG are both grounded whereas a voltage is applied to the top metal.

$$C_{\text{geo}} = \epsilon_0 \epsilon_r \frac{A}{d} \tag{2.5}$$

With A the area of the plates and d the distance between them [26].

In order to look at the capacitance of a mesoscopic system, such as a 2DEG, one can design the experimental setup shown in figure 2.7. The 2DEG is sandwiched between two metal layers. Now both the lower metal plate and the 2DEG are grounded. If the 2DEG would behave like a metal, only the geometrical capacitance between the top metal and the 2DEG could be measured. Furthermore, the 2DEG would shield the second metal plate completely from any electric field. However, experiments showed that the 2DEG does not screen the electric field completely, and the field partially penetrates the 2DEG. This experiment was done by S. Luryi in 1988 [27]. This leads to the conclusion that the capacitance of a capacitor, where at least one of the plates has a low density of states, is given by its geometrical capacitance and the second capacitance in series.

$$\frac{1}{C} = \frac{1}{C_{\text{geo}}} + \frac{1}{C_{\text{Q}}} \quad \text{with} \quad C_{\text{Q}} = e^2 D_T \tag{2.6}$$

C_{Q} is the quantum capacitance and is connected to the density of states D_T. e denotes the elementary charge. It can be seen, that if the DOS becomes large (classical limit) the total capacitance is again described by C_{geo} only. This renders the capacitance to be a suitable measure for the DOS of its plates [28].

2.3.1 Capacitance in a Circuit

By applying a DC voltage V_{DC}, charges move from one plate to the other one creating an electric field. Neglecting the quantum capacitance, C is a measure of how many charges can be stored on the plates at a certain applied voltage $Q = CV_{DC}$. While the charging process takes place, a current flows through the circuit, but it gets smaller with time, and as soon as the capacitor is fully charged, no current flows anymore. The capacitor blocks the DC current and needs to be discharged before it can be charged again.

An alternating current, which is applied to a capacitor, leads to continuous charging and discharging. Therefore, the capacitor acts like a resistance within this AC circuit. This resistance is called capacitive reactance X_C and depends on the frequency f (or angular frequency ω) of the applied AC voltage.

$$X_C = \frac{1}{\omega C} = \frac{1}{2\pi f C} \tag{2.7}$$

The capacitive reactance gets smaller with increasing frequency. If X_C goes to zero ($f \to \infty$) the capacitor acts like a wire with no resistance. In the limit of f approaching 0, X_C becomes large and approaches ∞. The case of a DC circuit is recovered, with the capacitor acting like an open circuit.

The complex impedance Z of the circuit is used to calculate its capacitance. Unlike an ohmic resistance, Z consists of a magnitude and a phase. It is a measure of an AC circuit combining any components of the circuit. These values can be measured using a lock-in amplifier, allowing the differentiation between the in-phase (real part, resistance, R) and the out-of-phase (imaginary part, reactance X) part. X usually has two parts to it, the inductive X_L and the capacitive reactance X_C. Since no inductors are used in the measurement circuit (see figure 3.5(a)), $X_L = 0$. Therefore, the reactance is purely capacitive $\mathrm{Im}(Z) = X_C$ and together with equation 2.7 the total capacitance of the measurement circuit can be calculated [26].

2.4 Magnetotransport of Electronic Systems

The classical Hall effect was first discovered by E. Hall in 1879 and is one of the most fundamental discoveries in physics. It can be observed on charges moving in a magnetic field. Due to the Lorentz force, negative and positive charges accumulate on opposite sides of the sample, leading to the Hall voltage. Over a century later, Klaus von Klitzing discovered that in a 2D charge system at low temperature, the Hall resistance does not depend linearly on the magnetic field anymore. It forms plateaus at distinct values, which can be directly related to fundamental constants [29]. The discovery of the quantum Hall effect was rewarded with the Nobel prize in physics.

2.4.1 Classical Hall Effect

When a current is applied from source to drain I_{SD}, the sides (perpendicular to the current) are at the same electrical potential, i.e. no voltage difference can be measured between these points $V_H = 0$. Edwin Hall discovered that with an external magnetic field perpendicular to the current, the two sides are no longer on the same potential, and a voltage difference between them can be measured, referred to as the Hall voltage V_H. This can be explained by the Lorentz force $\vec{F}_L$, which acts on moving charges in a magnetic field, as shown in figure 2.8.

$$\vec{F}_L = e(\vec{v}_D \times \vec{B}) \rightarrow F_L = e v_D B \tag{2.8}$$

Here v_D denotes the electrons drift velocity and e the elementary charge. The vector product is not necessary in this case since F_L, v_D and B are perpendicular to each other.

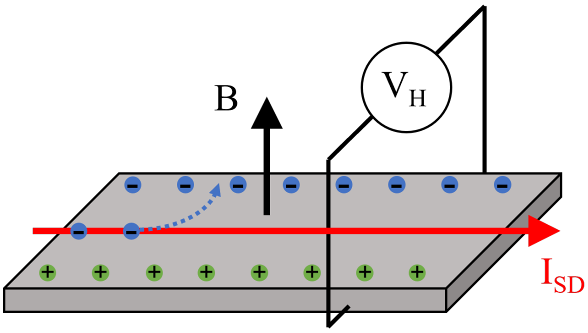

Figure 2.8: Schematic illustration of the classical Hall effect. Electrons (blue dots) are deflected due the external magnetic field and accumulate on the top side of the sample. This charge separation leads to a Hall voltage which is not zero.

This force causes the positive or negative charges to drift to one side of the sample, where they accumulate. This charge separation creates an electric field E, which builds up until the electrical force F_E equals F_L.

$$F_E = F_L \tag{2.9}$$

$$e\frac{V_H}{w} = ev_D B \tag{2.10}$$

$$V_H = v_D B w \tag{2.11}$$

where V_H is the measurable Hall voltage and w the width of the sample. The Drude model expresses the drift velocity as $v_D = I/(en_V A)$, with n_V being the volume density of the electrons and $A = d \cdot w$ the cross section of the sample. Therefore, the Hall voltage can be rewritten as,

$$V_H = Bw\frac{I}{en_V dw} \tag{2.12}$$

Using the two dimensional carrier density n, the Hall voltage can be expressed as,

$$V_H = \frac{IB}{en} \tag{2.13}$$

With this formula, the density of a 2DEG or 2DHG can be determined by a relatively simple measurement.

2.4.2 Quantum Hall Effect

The quantum Hall effect (QHE) was discovered by Klaus von Klitzing in 1980 [29]. He performed a Hall measurement using a 2DEG at low temperature (4.2 K). In his experiment, von Klitzing found that the Hall resistance R_H forms plateaus at discrete values of

$$R_H = \frac{1}{i}\frac{h}{e^2} \tag{2.14}$$

with i an integer number and h the Planck constant. An example of such a quantum Hall measurement can be seen in figure 2.9.

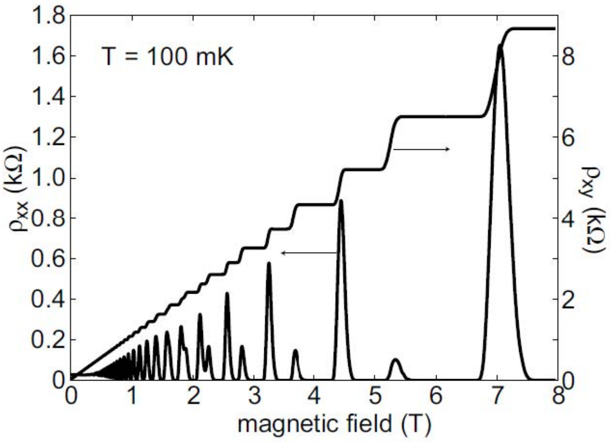

Figure 2.9: Measurement of the longitudinal ρ_{xx} and transverse ρ_{xy} resistance as a function of the magnetic field. The Hall plateaus are clearly visible as well as the Shubnikov-de Haas oscillation in ρ_{xx}. Figure from [18].

In order to understand the QHE, the motion of the carriers in the x, y plane has to be looked at. The magnetic field along the z axis, perpendicular to the charge carrierf system, forces the carriers to a circular motion. Solving the Schrödinger equation for this problem results in quantised energy levels, the Landau levels (LL). They are given by

$$E_j = \hbar\omega_C\left(j + \frac{1}{2}\right) \tag{2.15}$$

with j being the level index and $\omega_C = \frac{eB}{m^*}$ the cyclotron frequency. Therefore two neighbouring LLs are separated by $\hbar\omega_C$. As a consequence of this, the levels are more spaced out in bigger magnetic fields, leading to an emptying of the levels as they move above the Fermi energy. This is schematically shown in figure 2.10. The degeneracy of the LLs depends solely on B and is given by $n_L = \frac{|e|B}{h}$. The spin degeneracy of these levels can be lifted at high magnetic fields due to the Zeeman effect. The Zeeman energy gives the energy difference between these two sublevels

$$E_Z = sg^*\mu_B B \tag{2.16}$$

with g^* the effective g-factor, s the spin quantum number which can take values of ±1/2 and μ_B the Bohr magneton.

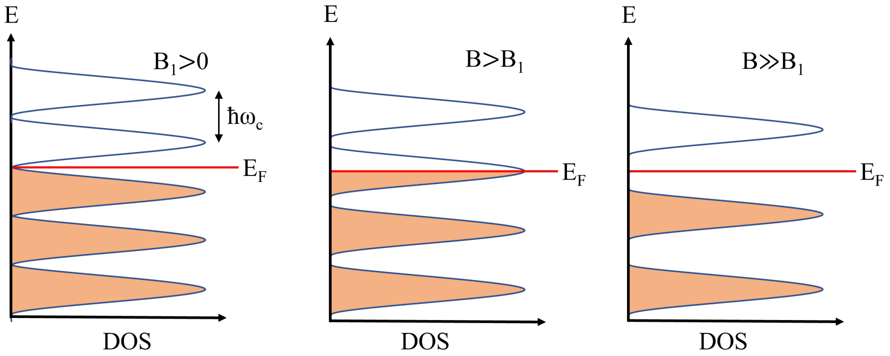

Figure 2.10: Schematic evolution of Landau levels with an increasing magnetic field. The levels are broadened due to thermal effects and scattering. Due to the increasing magnetic field, the LLs move upwards in energy and pass through the Fermi level. A half filled LL (middle scheme) allows transport through the sample. However, if E_F is in between two Landau levels, ρ_{xy} remains constant, resulting in the Hall plateaus. Figure adapted from [19].

Together with the carrier density of the 2D charge system n, the number of occupied Landau levels can be calculated:

$$\nu = \frac{n}{n_L} \tag{2.17}$$

$$= \frac{hn}{|e|B} \tag{2.18}$$

ν is called the filling factor. As an example, at $\nu = 1$ the first Landau level is half filled, i.e. the lower sublevel of the first LL is completely filled, while all other levels are empty.

The Landau levels can now be used to explain the quantum Hall effect. The formation of the LLs has a direct impact on the Hall resistivity ρ_{xy} on the sample. It becomes quantised as well and forms the plateaus at well defined resistance values of

$$\rho_{xy} = \frac{1}{\nu}\frac{h}{e^2} = \frac{1}{\nu}R_{\mathrm{K}} \tag{2.19}$$

with R_{K} the von Klitzing constant. The plateaus form when the filling factor ν is close to an integer number, therefore the name integer quantum Hall effect. In the measurements, it was also seen that the longitudinal resistance ρ_{xx} dropped to zero, which will be discussed in 2.4.3.

Fractional Quantum Hall effect

The name integer quantum Hall effect suggests that also a different QHE exists. Indeed, there is also the fractional quantum Hall effect (FQHE). In 1982 Tsui et al. found that the Hall resistivity also forms plateaus at fractional filling factors

[30]. In order to occur, the FQHE needs a very high quality sample and low temperatures. Otherwise, the thermal excitation of the electrons may screen the effect. The plateaus form at values of

$$\rho_{xy} = \frac{1}{p/q}\frac{h}{e^2} \tag{2.20}$$

with both p and q being integer numbers, and q has to be odd in (almost) all cases. There are some theoretical models for the FQHE, Laughlin's theory and the composite fermion model, which will not be discussed here. A more detailed explanation of the theory can be found in [18].

2.4.3 Shubnikov de Haas effect

As the Hall resistivity reaches its plateaus, the longitudinal resistivity drops to zero $\rho_{xx} = 0$, as seen in figure 2.9. In order to explain this, the broadening of the LLs has to be taken into account. In contrast to an ideal sample, a real sample contains crystal defects and impurities, which lead to scattering and to a broadening of the Landau levels. Additionally, they cause potential fluctuations in the 2D system. These fluctuations can form localised states, where carriers are confined in a potential minimum and do not contribute to the electrical current. The localised states are found in the tails of the broadened Landau levels. They connect the individual levels and allow the Fermi level to move through the LLs without changing the Hall resistivity. Around the centre of a LL, delocalised or extended states can be found. These extended states contribute to the conduction through the sample, thus changing the Hall and longitudinal resistivity. The resulting oscillations in ρ_{xx} are called Shubnikov-de Haas (SDH) oscillations. The SDH effect can be used to determine the charge density. The oscillations are periodic in $1/B$, and the separation between two neighbouring minima is given by

$$\Delta\left(\frac{1}{B}\right) = \frac{1}{B_{i+1}} - \frac{1}{B_i} = \frac{2e}{nh} \tag{2.21}$$

Here the factor 2 comes from the spin degeneracy of the LLs. If spin splitting is observed, this factor needs to be dropped [18].

2.5 Introduction to Tunnelling

Quantum tunnelling, or just tunnelling, is a phenomenon which is purely quantum mechanical. It describes the movement of a particle, with energy E, through a potential barrier with $V(x) > E$. In classical mechanics, the particle would need an energy larger than the potential barrier to pass it. A classical analogy would be throwing a handball against a solid wall, and the ball would go through it without destroying anything. This could be quite disturbing, but it happens in quantum mechanics on a regular basis.

One of the simplest models to describe the tunnelling effect is the model of a free particle tunnelling through a potential barrier with finite width and height. This model is taught in many undergraduate physics courses and can be found in various physics textbooks such as [31]. Therefore, the mathematical derivations are skipped, and the results are discussed straight away.

Figure 2.11 shows the tunnelling process of the model described above. It can be seen that the particle wave function inside the barrier experiences an exponential decay but does not go to zero. Therefore, the wave function can extend to the right side of the barrier, resulting in a non-zero probability of finding the particle there.

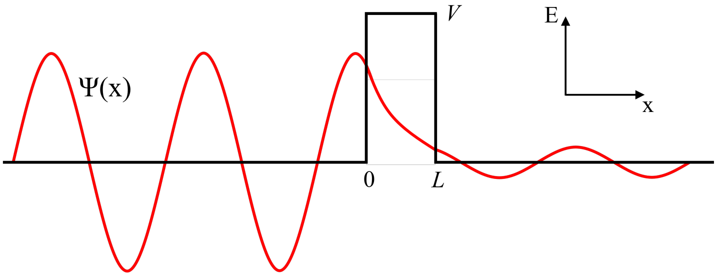

Figure 2.11: Tunneling of a free particle trough a potential barrier with width L and height V.

In semiconductors, this situation can be reproduced, e.g. by fabricating a high band gap barrier (e.g. AlGaAs) sandwiched between two low band gap regions (GaAs). Doped regions supply the structure with electrons or holes, which are accelerated by an external electric field and hit the barrier with energy E. In order to quantify the fraction of carriers tunnelling through the barrier, the transmission coefficient $T(E)$ can be used. It defines the probability of electrons (or holes) to tunnel through the potential barrier.

$$T(E) = \frac{1}{1 + \left(\frac{k^2+\alpha^2}{2k\alpha}\right)^2 \sinh^2(\alpha L)} \tag{2.22}$$

$$\text{with} \quad k = \frac{\sqrt{2m^* E}}{\hbar} \quad \text{and} \quad \alpha = \frac{\sqrt{2m^*(V-E)}}{\hbar} \tag{2.23}$$

L denotes the width of the barrier, V its potential height, E the energy of the electron (hole) and m^* the effective mass. This expression is only valid if the particles energy is smaller than the potential barrier $E < V$. The heavier the particle, the smaller its tunnel probability. Furthermore, $T(E)$ is larger for thinner barriers [20].

As bizarre as this phenomenon is, it is quite usual and can be found in various semiconductor devices, which might even appear in consumer electronics [32].

2.5.1 Resonant Tunnelling

One of the semiconductor devices mentioned above is called the resonant tunnelling diode. It consists of two barriers (AlGaAs) which enclose a quantum well (GaAs), sketched in figure 2.12(a). So far, only tunnelling of carriers into regions where there are no discrete energy levels was discussed. In this double barrier structure, the energy levels inside the quantum well are discrete, as shown in section 2.1.3. Solving the Schrödinger equation of this problem leads to a new form of the transmission coefficient [20]. Figure 2.12(b) shows $T(E)$ for this new potential structure.

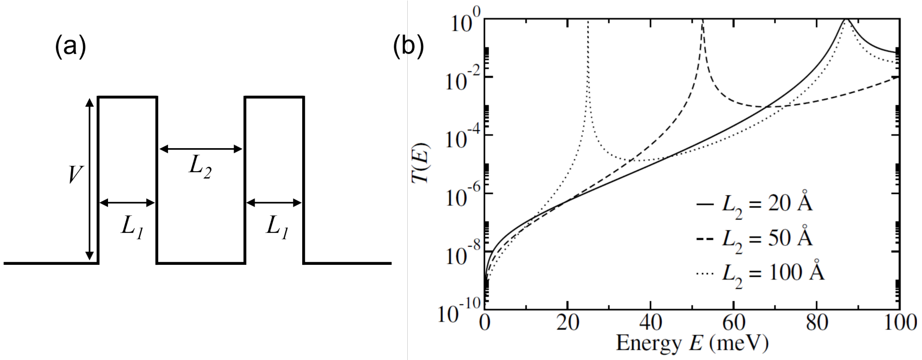

Figure 2.12: (a) Schematic of a structure with $V = 100\,\mathrm{meV}$ and $L_1 = 10\,\mathrm{nm}$. (b) Transmission coefficient for the double barrier case for an GaAs electron with $m^* = 0.067m_e$, for different L_2. The resonance peaks coincide with the energy levels of a quantum well with width L_2 (taken from [20]).

Unlike the single barrier case, the transmission coefficient contains maxima at energies below the potential barrier. At these energies, the transmission coefficient is 1, and the double barrier seems to be transparent. Furthermore, the energy at which these resonances occur matches the energy levels of a quantum well. This means that carriers which have the same energy as the resonance can pass through the barriers easily. In contrast, if they do not match the energy level, they are stopped at the barrier. This phenomenon is known as resonant tunnelling. One application is the quantum cascade laser, which was experimentally realised in 1994 by J. Faist et al. [33].

Resonant tunnelling can be suppressed by an in-plane magnetic field, meaning the magnetic field is within the plane of the quantum well. This was shown by J. Eisenstein et al. in 1991. In their work, they observed that the tunnelling conductance peaks at equal 2DEG densities, and can be reduced by applying a magnetic field parallel to the 2DEG plane [34].

Chapter 3

Experimental Methods

This chapter introduces the experimental methods used to synthesise the materials (Molecular Beam Epitaxy (MBE)) and fabricate the devices (clean room processing). It continues with an overview of the heterostructure of the measured p-i-n devices and closes with remarks on the measurement setup and procedure.

3.1 Molecular Beam Epitaxy

As the name already implies, the working principle of an MBE is to create a molecular (or atomic) beam of a source material that allows for well controlled growth on a crystalline substrate. This is achieved by heating high-purity materials in specially designed effusion cells. Figure 3.1 shows a schematic of an MBE system. The growth rates are usually less than one nanometre per second. This ensures precise control over the grown heterostructure in terms of material composition and layer thickness (down to a single monolayer).

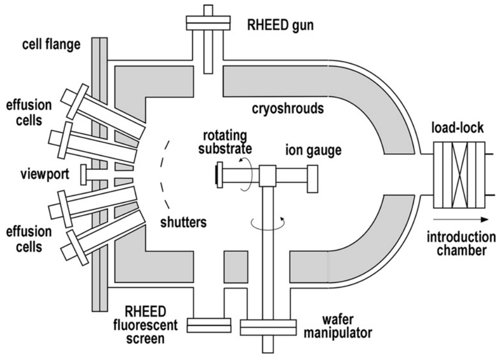

Figure 3.1: Schematic of the main chamber of an MBE-system. Figure from [35].

The growth process is carried out in an ultra-high vacuum chamber. The ultra-high vacuum (typically in the range of 10^{-12} mbar) can be converted to a mean free path in the order of hundreds of km, ensuring that the growth species can be delivered to the substrate surface without undesirable interactions. Secondly, the incorporation of background elements into the grown structure is reduced to a minimum.

The materials used in this thesis are the III-V semiconductors, GaAs and AlAs. This material system allows strain-free growth due to their similar lattice constant. For these materials, silicon usually acts as a donor and is used as n-doping. The counterpart, typically used to achieve p-doping, is carbon.

3.2 Semiconductor Heterostructures

In this section, the grown structures are discussed in detail.

The doping regions were grown using two different schemes, bulk or gradual doping. For bulk doping, the whole doping layer was grown with the same concentration of dopants. The gradual doping consists of five steps, which have a decreasing doping concentration, i.e. the concentration is the highest on the outer border and decreases gradually towards the intrinsic region (shown in figure 3.2). The typical width of the doping regions is ≈ 100 nm. The dopings were placed either in GaAs or in AlGaAs. The different combinations are shown below.

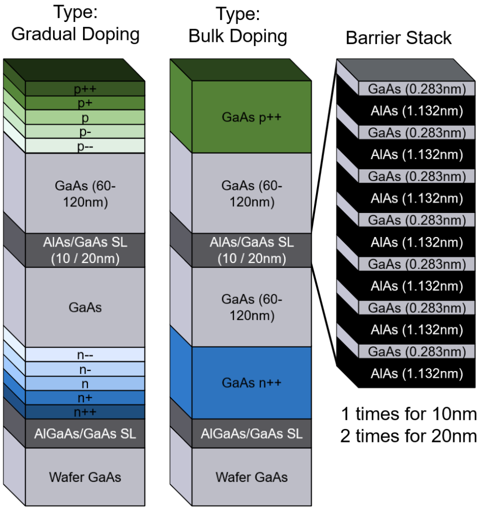

Figure 3.2: Sketch of the two doping schemes used in this thesis. The p- and n-doping were done either in GaAs or in AlGaAs. On the right side, the layer stacking of the barrier is shown. It is used in all samples and results in an overall composition of $Al_{0.8}Ga_{0.2}As$. Figure adapted from [15].

The intrinsic region was grown between the p- and n-doping. This part of the heterostructure dominantly affects the device behaviour. It consists of the $Al_{0.8}Ga_{0.2}As$ barrier, in the form of a digital alloy, encapsulated by undoped GaAs regions. To form the barrier, layers of 11.32 Å AlAs and 2.83 Å GaAs were grown in a repetitive order, until the desired thickness (between 10 and 20 nm, shown in figure 3.2) was reached. This design is adopted from ref. [36], where relatively high breakdown voltages were reported. The two adjacent GaAs layers act as quantum wells and host the studied bilayer system.

The main parameters which define the device behaviour are the barrier width (10 to 20 nm), the quantum well width (60 to 150 nm) and the quantum well structure (zero, single or double quantum well). The doping scheme does not influence the behaviour and it is omitted in the following discussions.

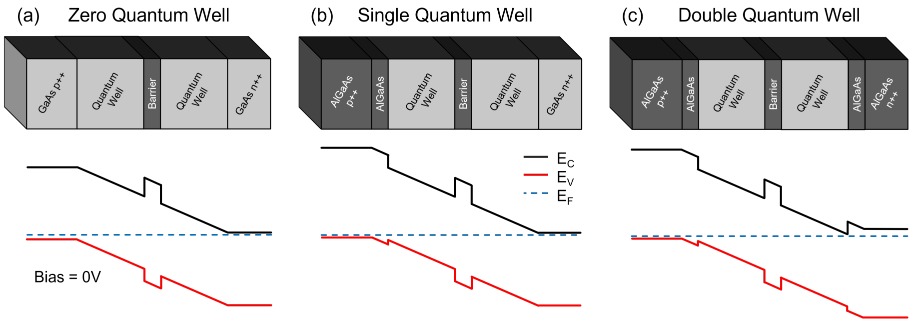

Figure 3.3: Schematic of the grown heterostructures as well as their band structure at zero bias. The doping scheme (bulk or gradual) is omitted since it did not influence the device behaviour.

The **zero quantum well structure** (shown in figure 3.3(a)) has both dopings placed in GaAs. This results, as the name suggests, in a structure with no real quantum well (no confinement). Even though the GaAs layers next to the barrier do not have any QW characteristics, they still will be addressed as such.

The **single quantum well structure** (figure 3.3(b)) has one real quantum well on the p-side of the barrier. This is due to the p-doping being placed in AlGaAs. Additionally, an undoped spacer of AlGaAs is grown between QW and p-doping. The n-doping remains in GaAs.

As the name implies, the **double quantum well structure** has a QW on either side of the barrier, as both dopings were placed in AlGaAs (shown in figure 3.3(c)).

3.3 Clean Room Fabrication

The grown heterostructure was further processed utilising optical lithography. Here, a short process overview is given, and the detailed recipe can be found in the appendix. The processing was done in FIRST[1], one of the clean room facilities of ETH.

In the first step, the mesas were defined by chemical wet etching. The targeted etch depth was optimised to access the n-doped region.

Secondly, the n-type ohmic contacts were patterned using optical lithography. The sample was dipped into HCl to remove any surface oxide in the contact region. Right after, the contact metals (Au/Ge/Ni) were deposited. A lift-off followed this. To ensure ohmic contacts (instead of e.g. Schottky contacts) the sample was annealed for 300 s at 470 °C.

Subsequently, the p-contacts were patterned directly on top of the mesa. An HCl dip was also done before depositing the contact metal (Pt/Ti/Au). After

---

[1] https://first.ethz.ch/

the lift-off, the samples had to be annealed to ensure ohmic contact with the p-doping. Since the p-contact is directly on top of the p-i-n device, the annealing temperature had to be low so as to not electrically shorten the device by the diffused metal. It was found that annealing for 30 s at 300 °C is sufficient, to obtain ohmic p-contacts.

In the last step, the samples were glued into chip carriers and wire bonded using a wedge bonding tool. Here, the p-contacts need to be bonded carefully, since in this design, they are located directly above the p-i-n device. Therefore, bonding power and time need to be optimised to not damage the underlying structure.

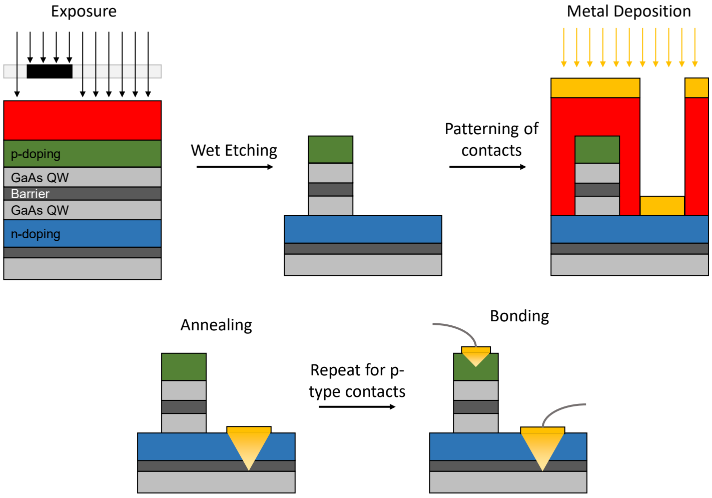

Figure 3.4: The different steps of the processing procedure.

3.4 Measurement Methods and Setups

This section presents the capacitance measurement and the analysis of the acquired signal. It continues with an overview of the cryostats used in this thesis.

3.4.1 Signal Acquisition

Figure 3.5(a) shows the capacitance measurement setup. An AC voltage is overlaid with a DC voltage. This allows to measure capacitance and to bias the device. It also can be seen that the circuit has two capacitance contributions, one from the device and one from the setup, which are connected in parallel.

In order to have a high measurement accuracy, the applied AC voltage V_{AC} needs to be small. Otherwise, too many data points are averaged, and small features do not show up in the data. This is simulated in 3.5(b), where 10 mV wide peaks with 20 mV spacing are shown.

The coloured curves represent the same data but with different binning widths (AC amplitude). For example, the red curve uses a bin width of 2 mV, i.e. the data point at 0 V averages the points from -2 mV to +2 mV.

This results in a reduced height of the peaks, but they are still resolved. If the excitation width is increased to 10 mV (blue curve), the measured signal does not represent the actual behaviour anymore. This is an example where the exciting (AC) amplitude is too large.

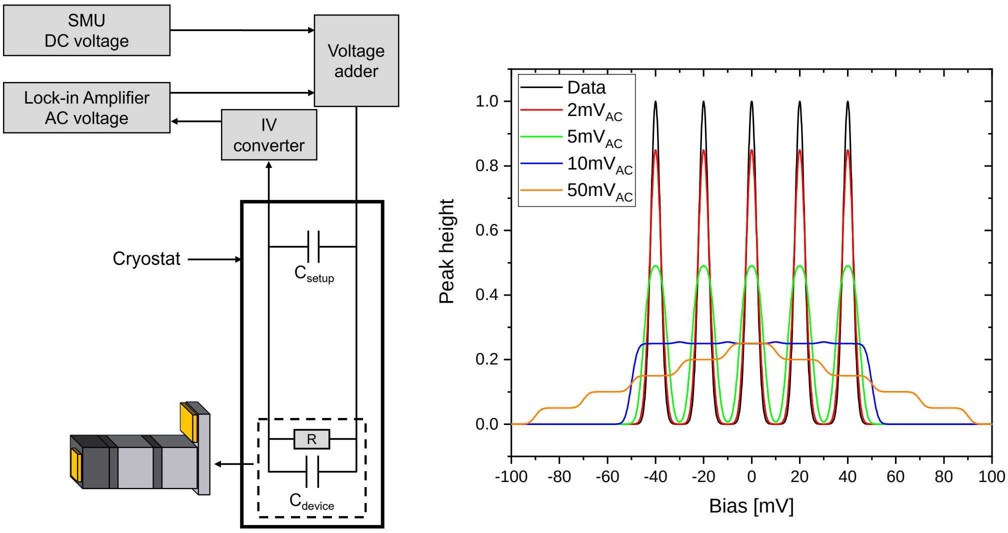

(a) Schematic of the measurement circuit.

(b) Simulation showing the impact of different AC amplitudes.

Figure 3.5: (a) Schematic of our measurement circuit with a device mounted. Figure from [15]. (b) Simulation showing the impact of different data averaging, i.e. AC amplitudes. The raw data is plotted as the black line. An amplitude up to 5 mV still reflects the characteristics of the signal, but the sharpness of the initial peaks is reduced. Above 5 mV (blue and orange line), the excitation is too big to resolve the initial peaks.

3.4.2 Signal Processing

A lock-in amplifier records the in-phase and out-of-phase signal simultaneously. The out-of-phase part is a measure of the total capacitance of our circuit (sample and cryostat). The in-phase component measures leakage and tunnelling through the barrier. Using the theory from section 2.3.1, capacitance can be calculated from:

$$\operatorname{Im}(Z) = \frac{V_{\mathrm{AC}}}{\operatorname{Im}(I_{\mathrm{sig}})} \tag{3.1}$$

$$= \frac{V_{\mathrm{AC}} R_f}{\operatorname{Im}(U_{\mathrm{sig}})} \tag{3.2}$$

where R_f is the adjustable feedback resistance and $\operatorname{Im}(U_{\mathrm{sig}})$ the out-of-phase signal. Since there are no inductive elements in the circuit, equations 3.1 and 2.7 can be combined to give:

$$\mathrm{Im}(Z) = X_C \tag{3.3}$$

$$\frac{V_{\mathrm{AC}} R_f}{\mathrm{Im}(U_{\mathrm{sig}})} = \frac{1}{2\pi f C} \tag{3.4}$$

Solving this equation for C results in

$$C = \frac{\mathrm{Im}(U_{\mathrm{sig}})}{2\pi f V_{\mathrm{AC}} R_f} \tag{3.5}$$

giving the capacitance of the whole measurement circuit C_{tot}.

The setup capacitance C_{setup} is parallel with the one from the device C_{device}, as shown in figure 3.5(a). Therefore, the device capacitance is calculated by subtracting the setup capacitance from the total one, $C_{\mathrm{device}} = C_{\mathrm{tot}} - C_{\mathrm{setup}}$. C_{setup} is extracted from a standard capacitance measurement with no device mounted.

3.4.3 Measurement Setups

To perform measurements at low temperatures, three different cryostats are used. Each of them has a different base temperature and cooldown time. First characterisation measurements are carried out in the cryostat with the shortest cooldown time. If these experiments show exciting results, the device is transferred to another cryostat with a lower base temperature.

Dewar Cryostat system: 4 to 1 K

The dewar system consists of a magnet rod mounted to a dewar and submerged in liquid helium. The hollow inside of the rod can be flooded by opening the needle valve at its bottom. At 4.2 K the coil is in a superconducting state and can produce magnetic fields up to 5 T.

The second component is the sample stick which was designed to fit inside the magnet rod and can hold two eight-pin carriers. The samples bathe in liquid helium at 4.2 K. Even measurements at temperatures down to 1.3 K are possible in this system. To reach the lower temperature, the needle valve is closed, and the magnet rod is evacuated. This reduces the boiling point of helium, and the samples are cooled down to 1.3 K.

The separation of the magnet from the sample stick allows a quick exchange of the carriers without warming up the magnet. This makes this system the most efficient for fast characterisations.

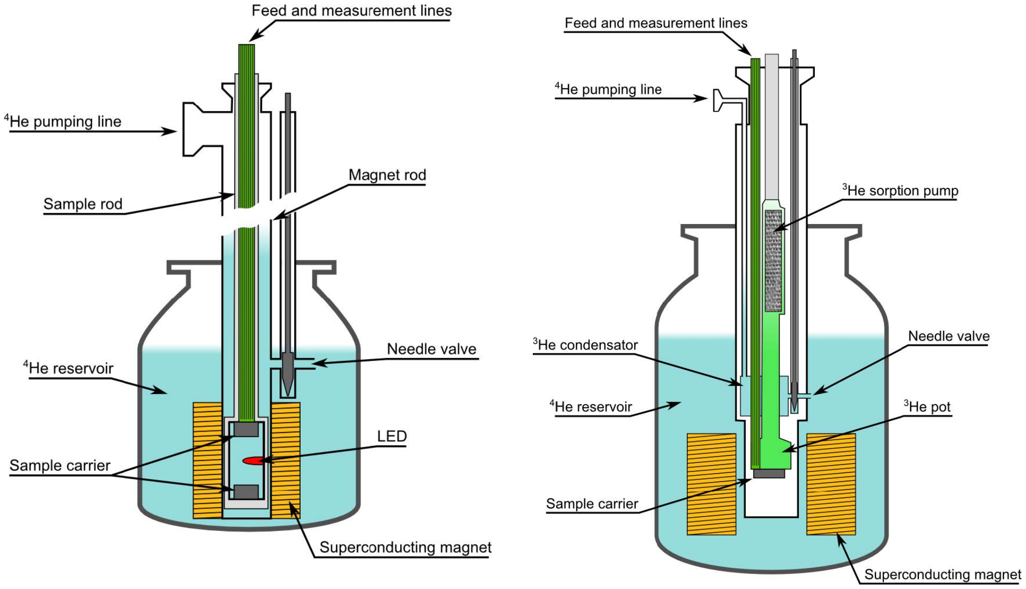

(a) Dewar cryostat **(b)** ^{3}He Cryostat

Figure 3.6: Schemes of the cryostats used in this thesis. (a) Dewar setup with a base temperature of 1.3 to 4 K. (b) ^{3}He evaporation cryostat with a base temperature of 250 mK. Figures from [19].

^{3}He Evaporation Cryostat: 250 mK

For measurements below 1 K, a ^{3}He cryostat is used. The working principle is similar to the one of the dewar system, just with ^{3}He instead of ^{4}He. The boiling point of ^{3}He lies at 3.5 K at atmospheric pressure and at 0.25 K in vacuum. To condense the ^{3}He in the condensator (shown in figure 3.6(b)), ^{4}He at 1.3 K is used. By pumping on the liquid ^{3}He, a base temperature of 0.25 K can be reached. The cooling power is provided until all liquid ^{3}He is evaporated, then it has to be condensed again. This limits the measurement time at base temperature to 20 hours, which is further reduced when measurements in a magnetic field are performed. The magnet of this system is capable of producing fields up to 14 T. In order to reduce the thermal load from the surroundings, the whole system is submerged in liquid ^{4}He, which has to be refilled every 3 to 4 days. This pot also serves as a reservoir for the condensator.

Dilution Refrigerator: 25 mK

To measure samples at millikelvin temperatures, a dilution refrigerator is used. This system works with a mixture of ^{3}He and ^{4}He. Unlike in the system described above, the cooling power in this setup does not come from evaporation but from a phase transition between ^{3}He and a mixture of both isotopes.

Cooling such a mixture down results in two phases, a diluted (approximately 6.4% ^{3}He) and a concentrated one (almost pure ^{3}He). These phases do not mix and are separated in the mixing chamber of the cryostat. By pumping on the diluted phase, only ^{3}He is removed. To contain the constant fraction of 6.4% ^{3}He, there is a flow of ^{3}He through the phase boundary. The cooling power results from this phase transition since it is endothermic and draws the required energy from the surrounding. The evaporated ^{3}He is cleaned in a cool-trap which sits in liquid nitrogen and is fed back to the mixing chamber. Since the evaporation and condensing of ^{3}He is a continuous process, this system allows uninterrupted measurements at a base temperature of 25 mK. This cryostat is equipped with a magnet that produces fields up to 12 T.

With theoretically unlimited measurement time and low regular maintenance (refilling the cooling trap every 7 days with liquid nitrogen), this system also has some drawbacks. It is more costly to run (compared with the other two systems), and it takes up to 3 days to cool a sample to base temperature.

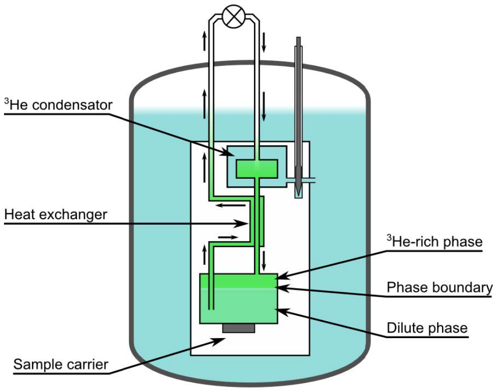

Figure 3.7: Dilution refrigerator with a base temperature of 25 mK. Figure from [19].

Chapter 4

Characterisation and Results of weak interacting 2DESs (20 nm-Barrier)

This chapter starts with an overview of the measurement method and shows how different parameters influence the measured results. It continues with experimental results on samples with a 20 nm thick barrier.

4.1 Characterization and Measurement

4.1.1 General Method

With an applied AC voltage, it is possible to probe the capacitance of the circuit. By superimposing the AC with a DC voltage, the charge carriers can be moved towards the barrier, where they accumulate. This changes the distance between the charges and leads to a change in capacitance. Therefore, four different regimes should be distinguishable in a bias sweep (shown in figure 4.1).

1. Regime I *Bulk*: at low bias, the charges are located in the doping layers. This results in a large distance between them and therefore in a small capacitance.

2. Regime II *Step*: at a certain threshold voltage V_{th}, the charges move from the doping layers into the quantum wells and accumulate next to the barrier. Here they form the two 2DESs. This results in a step-like increase in capacitance.

3. Regime III *Plateau*: above V_{th}, the capacitance saturates and evolves into a plateau. C still can increase due to the squeezing of the carrier wave functions and the increase of carrier density.

4. Regime IV *Breakdown*: if the applied voltage exceeds V_{br}, the carriers have enough energy to overcome the energy gap of the barrier. This leads to an increase in conductance, which is picked up as the in-phase signal.

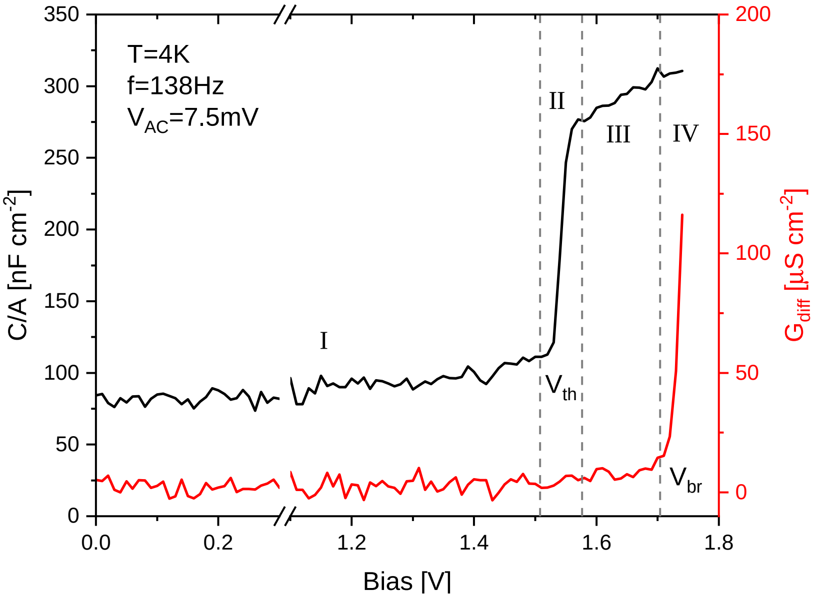

Figure 4.1: Full sweep of a sample with a 20 nm thick barrier. The capacitance stays almost constant until V_{th}, regime I. In regime II, the capacitance experiences a step-like increase due to the formation of the two 2DES close to the barrier. In regime III, C increases due to a change of density and squeezing of the wave functions. Above V_{br}, regime IV starts.

4.1.2 Effect of Changing AC-Amplitude

The out-of-phase signal is modified by the amplitude and frequency of the AC voltage. It was already discussed in 3.4.1 that the amplitude needs to be small compared to the features in the measurement. Since the measured signal is directly coupled to the applied AC amplitude, a reduction in amplitude leads to a smaller signal. The measurement series in fig. 4.2 demonstrates this behaviour. It can be seen that the threshold voltage varies a lot between the lowest (5 mV) and highest (100 mV) amplitude. Furthermore, the plateau from regime III is not resolved above 25 mV. Figure 4.2 shows also that the noise level increases with decreased excitation. In order to have a high accuracy in the measurements, the amplitude was set to the smallest value, which had a bearable noise level.

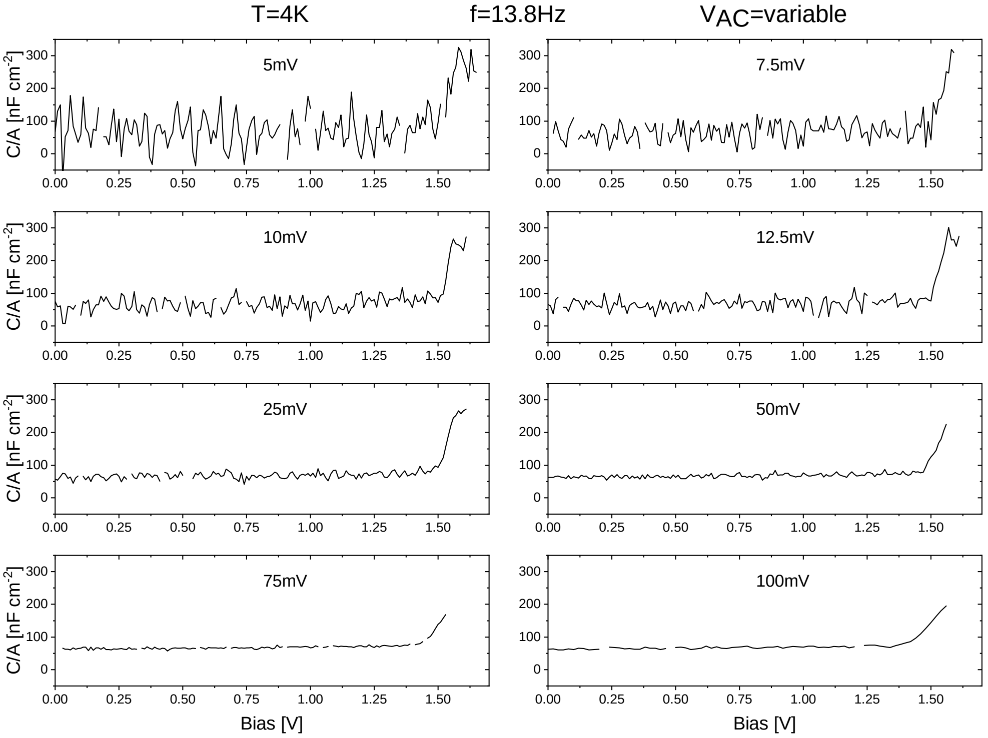

Figure 4.2: Measurement series of a device with a 20 nm thick barrier. The temperature and frequency were kept constant for all measurements, only the applied V_{AC} was changed. It can be seen that at higher applied amplitude, the capacitance plateau is not resolved anymore. On the other hand, low excitation leads to a poor signal-to-noise ratio.

4.1.3 Effect of Changing AC-Frequency

The second variable of the AC excitation, besides the amplitude, is its frequency f. Measurements with varying frequencies but the same amplitude were carried out. By increasing f, the signal increases as well, but the capacitance remains constant (shown in figure 4.3). The measurements were limited to a frequency range between 30 Hz and 1 kHz. Within this range, the behaviour of the capacitance is stable and only varies by a few percent. This proves that the charges behave similarly at all frequencies or, in other words, they move from doping to barrier and back with no delay.

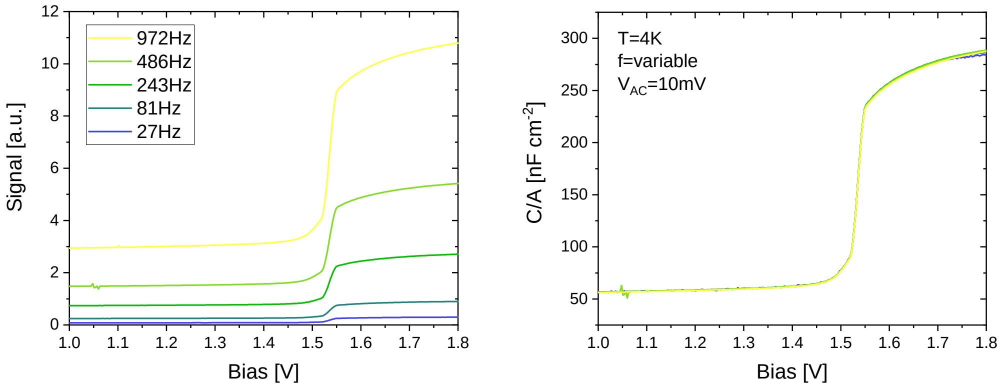

(a) Measurement Signal **(b)** Calculated capacitance

Figure 4.3: Measurement series of a device with a 20 nm thick barrier. The temperature and V_{AC} were kept constant for all measurements. The measured signal depends strongly on the frequency of the applied AC voltage whereas the capacitance is unaffected by it.

The combination of low amplitude ($< 25\,\text{mV}$) and reasonably high frequency ($\approx 200\,\text{Hz}$), provides results with a sufficient accuracy at a tolerable noise level. Since the measuring setups used in this work have different internal noise, the frequency-amplitude combination was chosen individually for each measurement. Therefore, the data shown in this thesis are provided with the used combination.

4.1.4 Effect of Different Contact Coverages

In order to normalise the measured capacitance to one cm^2, it is crucial to know the active area of the device. There are two possible options, either the area is defined by the etched region or the contact metal. Figure 4.4(a) shows an optical image of the sample used in this experiment. Both devices shown have the same area (red circle in figure 4.4(a)), but different fractions are covered with contact metal (blue (quarter)circle in figure 4.4(a)). Since the surface layers are doped to a degenerate level, it is assumed that the contact area (metal coverage) does not change the measured capacitance.

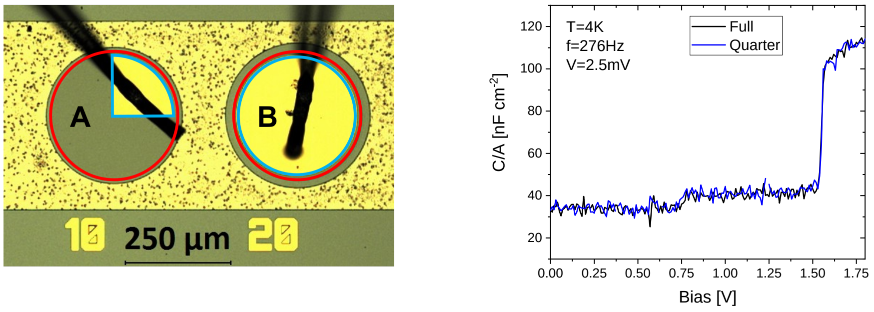

(a) Optical image of the two samples.

(b) Measured C of the devices in (a)

Figure 4.4: (a) Optical image of the two devices measured. Both capacitors have the same etched region (inside of the red circle). A has only a quarter of it covered with contact metal (inside of the blue quarter), whereas in B almost the whole device is covered by the contact. The black lines are the bonding wires and the grainy area outside the capacitors is the n-type contact metal. (b) Measurement of the two samples. Both capacitors have the same progression and value of capacitance. The small plateau at 0.75 V will be discussed in the next section.

Figure 4.4(b) shows the measurement of the two devices. Both capacitors show the same behaviour and value of the capacitance. This result suggests that the area of the device is defined by the etched region and not by the coverage of contact metal. Therefore, the etched area was used in the analysis of the capacitance.

4.1.5 Effect of Different Heterostructures

This paragraph discusses the influence of the different heterostructures, which were presented in 3.2, on the capacitance. The analysis focuses on the behaviour below the threshold voltage (regime I *Bulk*). Discussions above V_{th} can be found in sections 5.1 and 5.4. The samples shown in this paragraph have a 10 nm barrier and either a 90 or 120 nm quantum well. The width of the well or barrier does not change the behaviour discussed here.

In order to compare the three structures, they are normalised to the capacitance at zero bias. Figure 4.5 shows that below 0.75 V all structures behave similar. They have a small but steady increase in capacitance. This growth of C can be attributed to an

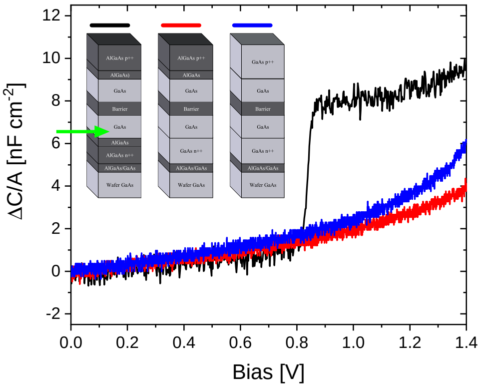

Figure 4.5: Behaviour of C in regime I *Bulk* for the three heterostructures used in this thesis. The inset shows schemes of the structures. It can be seen that both devices with the Si doping in GaAs (blue and red line) behave similar, whereas the device with the n-doping in AlGaAs (black line) has a step-like increase at 0.75 V.

increase in the electron density at the border between the Si doping and the quantum well.

Above 0.75 V the device with both dopings placed in AlGaAs (double quantum well structure, black line) develops a plateau which is unique to that heterostructure. The other two structures, with the n-doping in GaAs (zero or single quantum well structure), show a continuous C increase. The step in the black curve originates most probably from electrons accumulating in the QW at the outer border (green arrow in figure 4.5).

4.2 Experimental Results of weak interacting 2DESs (20 nm-Barrier)

4.2.1 Capacitance

This chapter shows experimental results from devices with a 20 nm thick barrier or, in other words, have low interaction strength between the two 2DESs at the barrier. Figures 4.6(a) and 4.6(b) show the measured data of samples which have both dopings in GaAs (device A, zero quantum well structure[1]) or AlGaAs (device B, double quantum well structure) respectively.

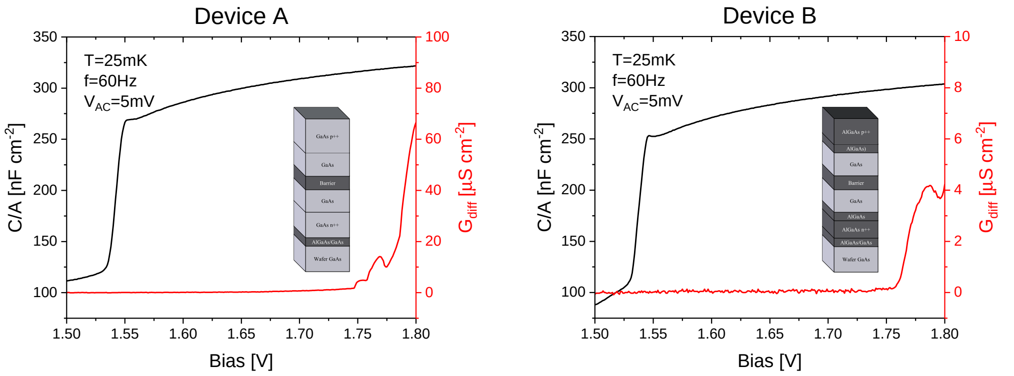

(a) Device A, zero quantum well structure. **(b)** Device B, double quantum well structure.

Figure 4.6: Both samples show the expected capacitance plateau and are leak tight up to 1.75 V. The measurement was aborted at 1.8 V to prevent any damage to the samples. Figure adapted from [15].

In device A (figure 4.6(a), zero quantum well structure) the capacitance plateau forms above V_{th} and no leaking current up to 1.75 V applied bias is observed. This shows that the barrier is indeed tight. Above the breakdown voltage, the carriers have enough kinetic energy to overcome the potential barrier. The capacitance plateau is slightly smaller than the geometrical value $C_{\text{geo}} = 339\,\text{nF}/\text{cm}^2$, which is calculated from simulations where the two 2DESs formed close to the barrier.

---

[1] The undoped GaAs regions next to the barrier are referred to as quantum wells, even though they do not have any quantum confinement.

This agrees with the assumption that the geometrical and quantum capacitance are connected in series. Therefore, the total capacitance of both contributions results in a value smaller than C_{geo}.

Device B (figure 4.6(b), double quantum well structure) shows the same characteristics as device A. There is no leakage up to 1.75 V bias, and the capacitance plateau is lower than the geometrical value.

4.2.2 Magneto-Capacitance

Within the same measurement series, experiments with an applied perpendicular magnetic field were also performed. The B-field did not change the behaviour of the capacitance up to $\approx 250\,\text{mT}$. Above this field strength, magneto-oscillations can be seen. In device A, the threshold for observing magnetic effects is even higher. This can be seen in figure 4.7.

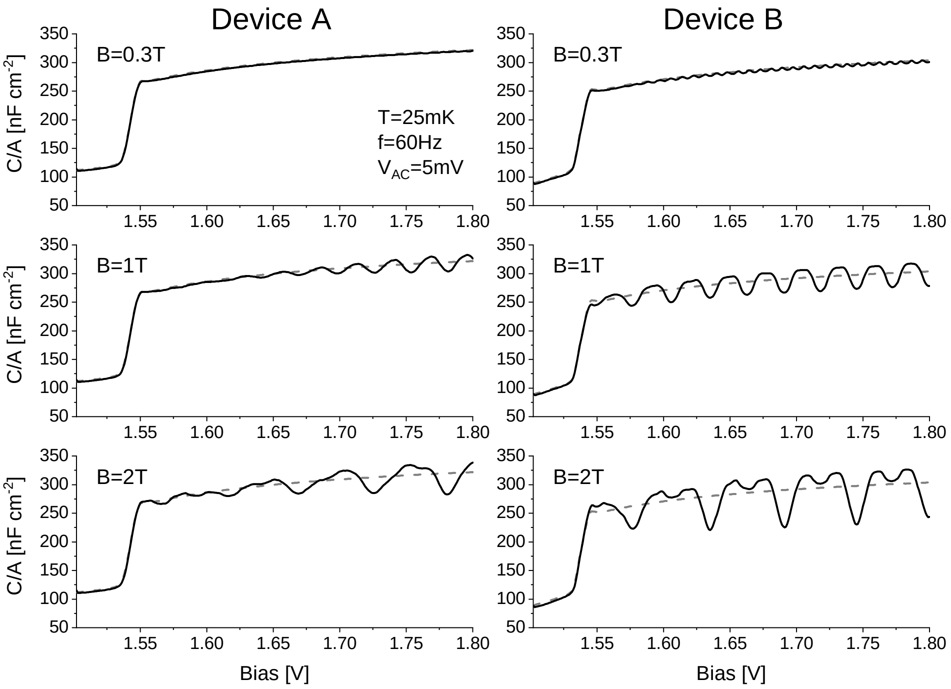

Figure 4.7: Bias sweeps at different magnetic fields. The grey dashed line depicts the capacitance curve at zero magnetic field, whereas the black solid line shows the measurement at the denoted field. Device A does not show any clear magneto oscillation at 300 mT. However, these are already visible in device B at this magnetic field. At a magnetic field of 2 T, a second kind of magneto-oscillation is observed. Figure adapted from [15].

The minima are due to the Landau quantisation of the 2D systems. The Landau levels are swept through by either increasing the magnetic field or the density of the 2DES (with the applied bias). This changes the density of states available at the barrier. If the parameters are set such that the Fermi level is between two LLs, the density of states is low, and a minimum in capacitance is observed. In other words, since there are no free states in the 2DES at the barrier, the carriers cannot enter the charge system. Therefore, reduced capacitance is measured.

A closer look at figure 4.7 shows that at higher B-fields ($B > 2\,\mathrm{T}$) the shape of the oscillations changes. Especially in device B, it can be distinguished between two kinds of Landau oscillations, shallow and deep ones. The shallow minima only start to show up at higher magnetic fields, where spin splitting must be considered. The deep minima are assigned to even and the shallow ones to odd filling factors. The difference between the two shapes is rather visible in B. This can be explained by taking a look at the heterostructure. In device A, the doping layers end directly next to the quantum wells, which can degrade the quality of the 2D systems. In contrast, device B has an undoped 30 nm spacer grown between the doping layers and the quantum well. This seems to increase the quality of the 2DESs.

Bias sweeps for magnetic fields up to 12 T were recorded, the full data can be seen in figures 4.8(a) (device A, zero quantum well structure) and 4.8(b) (device B, double quantum well structure). Both samples show a clear Landau fan. It is even possible to observe faint oscillations due to the fractional quantum hall effect.

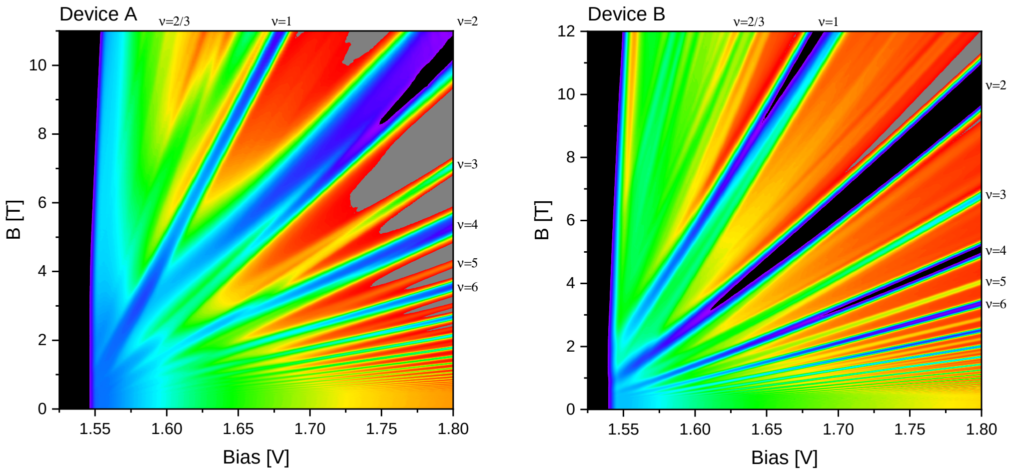

(a) Device A, zero quantum well structure. **(b)** Device B, double quantum well structure.

Figure 4.8: Capacitance as a function of magnetic field and bias. Both devices develop a Landau fan. The even and odd filling factors can be distinguished. Hints of the fractional quantum hall effects are visible at high magnetic fields.

Since only one Landau fan and not two overlapping ones are observed, it is assumed that the two charge systems have the same carrier density. Figure 4.9 shows a linear dependence of the density on the applied bias. Due to the lack of undoped AlGaAs spacer (between the QW and doping), device A has a higher density than device B. The total tunable range reaches from 0.5×10^{11} up to $5 \times 10^{11}\,\mathrm{cm}^{-2}$.

The measurements without a magnetic field imply that two charge systems close to the barrier are created. Otherwise, the capacitance plateau in figures 4.6(a) and 4.6(b) would saturate at a lower level. Measurements with an applied magnetic field support that at least one of the two systems at the barrier is in a 2D state. However, both systems are assumed to behave like a 2D gas of carriers with equal densities.

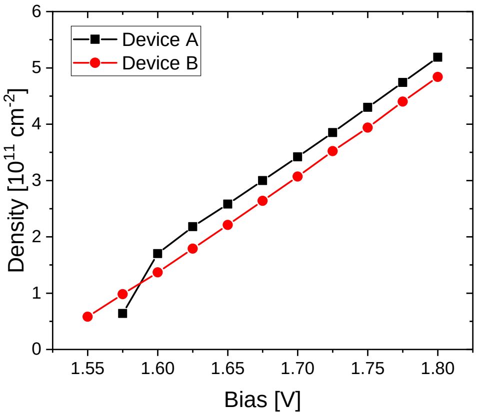

Figure 4.9: The density of both devices scales linearly with bias, only the point of device A at 1.575 V differs from this behaviour.

Chapter 5

Experimental Results from strong interacting 2DESs (10 nm-Barrier)

The reduction of the barrier width down to 10 nm leads to an increased interaction strength between the charge layers at the barrier. This chapter starts with experiments on devices with both dopings in GaAs (zero QW structure). By changing the background material of the p-doping to AlGaAs (single QW structure), new oscillations in capacitance can be observed. They also occur if both dopings are placed in AlGaAs (double QW structure). The changed background material of the p-doping turns out to be the origin of the newly observed oscillations.

5.1 Zero Quantum Well Structure

Measurements of devices with a 10 nm-barrier and both dopings placed in GaAs (inset in figure 5.1(a)), show similar characteristics as the ones with a 20 nm thick barrier. Figure 5.1 shows the onset of the capacitance plateau as the two 2DESs form at the barrier. Since they have a smaller distance between them, the capacitance saturates at a higher value. This plateau is close to the geometrical capacitance $C_{\text{geo}} \approx 480\,\text{nF/cm}^2$, which is expected for the two 2DESs forming at the barrier. Furthermore, an increased in-phase current from tunnelling can be observed.

With an applied perpendicular magnetic field, the formation of Landau levels in the capacitance can be observed. Figure 5.1(b) shows, that at 0.2 T capacitance-magneto-oscillations appear.

As in section 4.2.2, even filling factors can be assigned to the deep oscillations and odd fillings to the shallow ones caused by spin splitting. With increasing magnetic field, both (even and odd) minima become more pronounced. Figure

5.2(a) shows the complete measured range. The observed Landau fan shows weak hints of fractional filling factors.

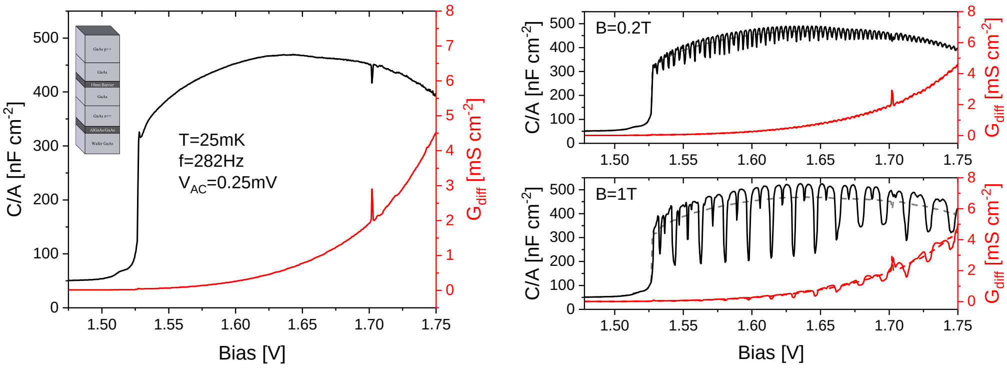

(a) C and G_{diff} at B=0 T

(b) C and G_{diff} at two different B-fields.

Figure 5.1: Data recorded of a device with a 10 nm thick barrier and a zero quantum well structure with 120 nm wide QW. The structure at 1.7 V is most probably due to tunnelling through an electrical level in the barrier. (a) No magnetic field applied: C reaches approximately the expected geometrical value. (b) Measurements at two chosen magnetic fields. Spin splitting can be observed at higher fields.

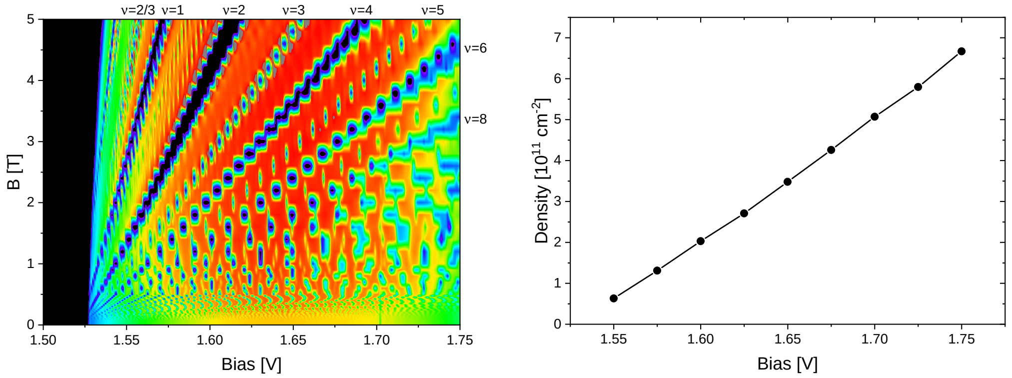

(a) C as a function of bias and B-field.

(b) Density as a function of bias.

Figure 5.2: (a) Capacitance as a function of bias and magnetic field. The point like appearance of the Landau fan is due to finite magnetic field step size during the measurement. Spin splitting and fractional fillings factor can be identified. (b) The density scales linearly with the applied bias.

The density, shown in figure 5.2(b), scales linearly with the applied bias and can be tuned from 0.6×10^{11} up to $6.5 \times 10^{11}\,\mathrm{cm}^{-2}$.

The zero QW device, with the 10 nm thick barrier, does not show significant differences compared to the 20 nm-barrier devices. However, from these measurements, it is concluded that the measurement methods still work with the new barrier width.

5.2 Capacitance Oscillations and Resonant Tunnelling

This section continues with the discussion on samples with a 10 nm thick barrier. However, the carbon doping was placed in AlGaAs rather than in GaAs. This results in a wide quantum well on the p-doped side of the barrier. On the other side of the barrier, no quantum well forms due to the n-doping remaining in GaAs (single quantum well structure). Figure 5.3 shows the completely new phenomena observed in this device.

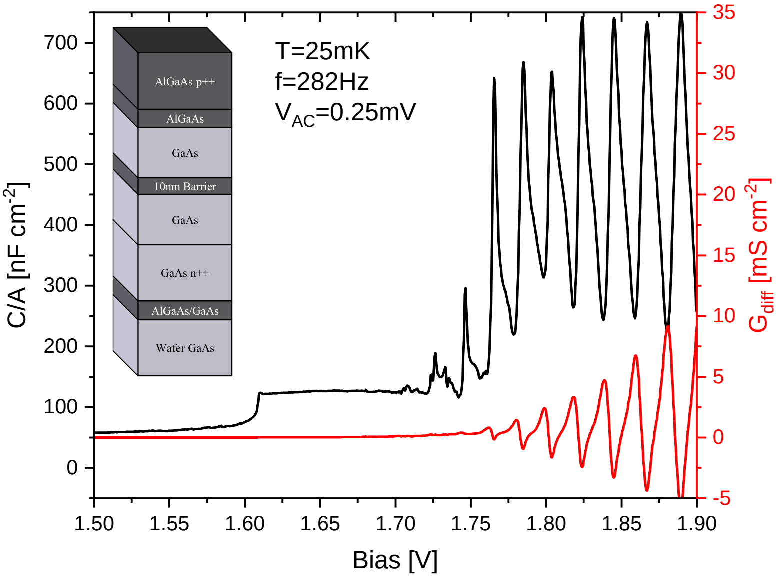

Figure 5.3: The inset shows the structure of the device used for this measurement. The quantum well has a width of 90 nm. The oscillations above 1.7 V are new and surprising since they occur in the absence of any magnetic field. Furthermore, the peak capacitance exceeds the theoretical geometric value of 480 nF/cm^2. Figure adapted from [15].

A much more striking feature of these measurements are the oscillations in the capacitance and differential conductance above 1.7 V. Capacitance oscillations have already been seen before (e.g. figure 5.2(a)), but these new ones form in the absence of an applied magnetic field. Another characteristic is the regularity of the peaks. The peak-to-peak distance does not change within the measured range, they are equidistant. Furthermore, these oscillations are very robust and turn out to be rather hard to manipulate.

5.2.1 Resonant Tunnelling

The experimental results imply that the origin of the oscillations is connected to tunnelling into discrete levels. Resonant tunnelling (RT) of electrons is suggested to be the cause of the oscillations.

With this model, the following picture is drawn. Electrons from the ground state of the triangular well E_0^n tunnel into unoccupied levels (index m) on the left (p-doped) side[1] E_m^p. Tunnelling is maximal when the occupied energy level on the n-side E_0^n is at the same energy as one of the unoccupied levels on the p-side of the barrier $E_0^n = E_m^p$. Tunnelling of holes is neglected due to their heavy mass.

Figure 5.4(a) shows a simulation of the conduction and valence band. The equal spacing of the oscillations might contradict the model at first since, at zero bias the quantum well on the p-side is square-shaped. This would result in an m^2 behaviour of the energy levels. In other words, the energy difference between neighbouring levels increases with increasing level number m. Accordingly, the measured peaks would not be equally spaced.

However, experiments always showed an equal spacing of C and G_{diff} peaks. This indicates parabolic confinement, as in a harmonic oscillator, where the energy levels are equally spaced. By taking the two 2DHGs into account (figure 5.4(a) red curve), it can be seen that the valence band is deformed towards parabolicity. Furthermore, the voltage dependence of the energy levels was considered as well.

Using the simulation software *Nextnano* [37], the energy levels on both sides of the barrier were calculated for a series of applied bias. The bias values, when the energy level of the ground state on the right side (n-doped) coincides with one level of the p-side quantum well, $E_0^n = E_m^p$, were extracted. This results in the effective level spacing with applied bias, shown in figure 5.4(b). At low bias and level number m, a quadratic behaviour of the energy levels can be seen. However, at the experimental relevant bias (between 1.7 V and 1.9 V) the calculated energy levels become approximately equally spaced, which is in agreement with the experiments.

---

[1] Please note the notation of the energy levels: $E_{\text{level index}}^{\text{p-/n-doped side}}$, e.g. E_0^p denotes the ground level on the p-doped side of the barrier.

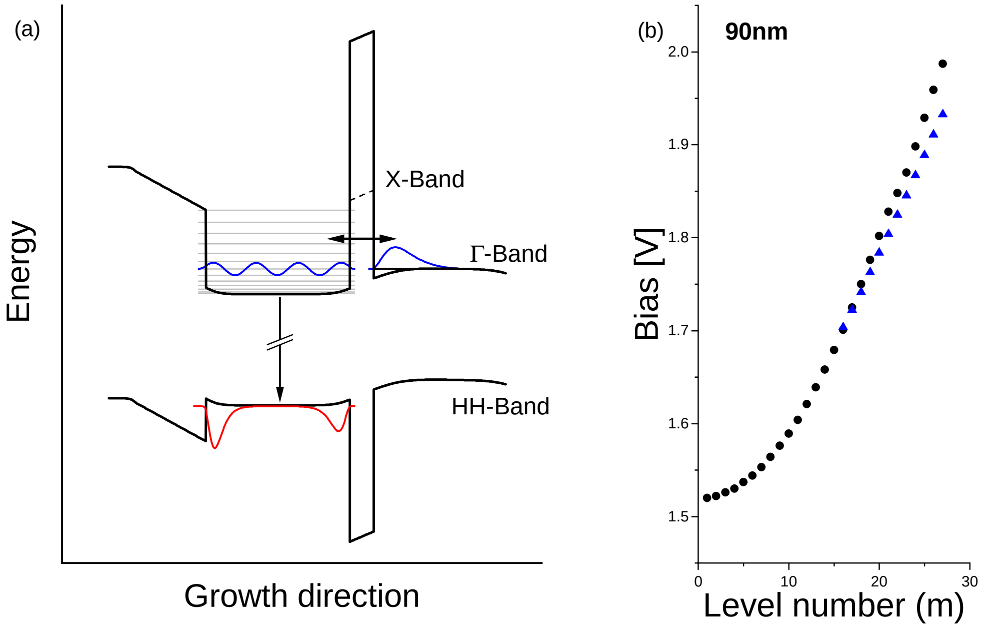

Figure 5.4: (a) Simulated model for resonant tunnelling. The energy levels of the left side quantum well E_m^p are drawn as grey lines. Right from the barrier only the ground state E_0^n is occupied. The hole gases (red line) in the valence band deform the square well. (b) The black dots denote simulated level alignment $E_0^n = E_m^p$, which indicates the voltages resonant tunnelling would be expected. The experimental peak positions are plotted as blue triangles and match the simulation quite well. Figure from [15].

A linear fit of the simulated data (figure 5.4(b)) within the experimentally relevant bias range (1.7 V to 1.9 V) finds a theoretical voltage period of 25.7 mV for a sample with a 90 nm wide quantum well. This is slightly larger than the experimental observed period of 20.4 mV. The experimental data (blue triangles) are also shown in figure 5.4(b). The starting index number was chosen to best fit to the low-voltage data points.

The following part of this chapter presents experiments that support the model and measurements that cannot be explained with resonant tunnelling.

5.3 Further Experiments on Single Quantum Well Structures

To verify the resonant tunnelling picture, series of measurements were carried out, which are presented in this section. Unless stated, all experiments mentioned were done with single quantum well devices containing a 10 nm-barrier, i.e. the p-doping in AlGaAs and the n-doping in GaAs.

5.3.1 I-V Characteristic

In order to rule out whether the oscillations originate from the measurement circuit or the AC-excitation, the IV characteristic of the device was measured. A DC voltage was applied directly to the p-contact, whereas the n-contact was put on ground. No voltage adder or lock-in amplifier was used. The SMU functions within this configuration as a current meter. The device used in this paragraph had a single quantum well (120 nm width) on the p-side of the 10 nm thick barrier.

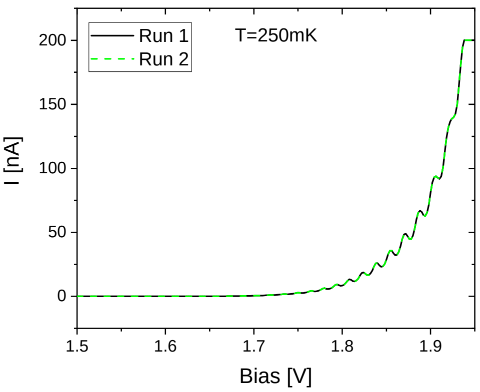

Figure 5.5: IV characteristic of a sample with a 10 nm thick barrier and a quantum well width of 120 nm. The two sweeps shown in the graph, lie almost perfectly on top of each other. The plateau at 200 nA is due to the compliance of the SMU.

As is shown in figure 5.5, no current is observer up to 1.7 V. This corresponds to the AC measurement from figure 5.3. Here G_{diff} is also close to zero within the same bias region. Above 1.7 V the current in figure 5.5 starts to rise and shows peaks which correspond to the oscillations seen before. Please keep in mind that the oscillations appear less pronounced than in the other figure, which showed the differential data.

These measurements rule out that the effect originates from the measurement setup or is an artefact of the applied AC voltage. Furthermore, the effect is reproducible. Two measurement runs are shown in figure 5.5, which lie almost perfectly on top of each other.

5.3.2 Variation of AC-Frequency

Another series of measurements was done to study the oscillations with different AC-frequencies. It is known from other experiments (section 4.1.3), that changing frequency only affects the capacitance signal, but not C or G_{diff}. Therefore, it is assumed that any changes to the oscillations will not come from the measurement method but from the phenomenon itself. The measurements in figure 5.6 show a series of experiments, in which the frequency varies between 80 and 1000 Hz. The series was carried out using a single quantum well device with a 10 nm-barrier and a 90 nm wide quantum well.

Two regimes can be distinguished in the graphs. The first one located between 1.7 V and 1.8 V. In this bias region, the capacitance peaks at lower frequencies are more pronounced. In order to understand this effect, it needs further studies. Above 1.8 V neither C nor G_{diff} are affected by the applied frequency. However, the oscillation period is unaffected by frequency in both regimes. The work done in this thesis focuses mainly on the period, therefore it is assumed that the oscillations are independent of frequency.

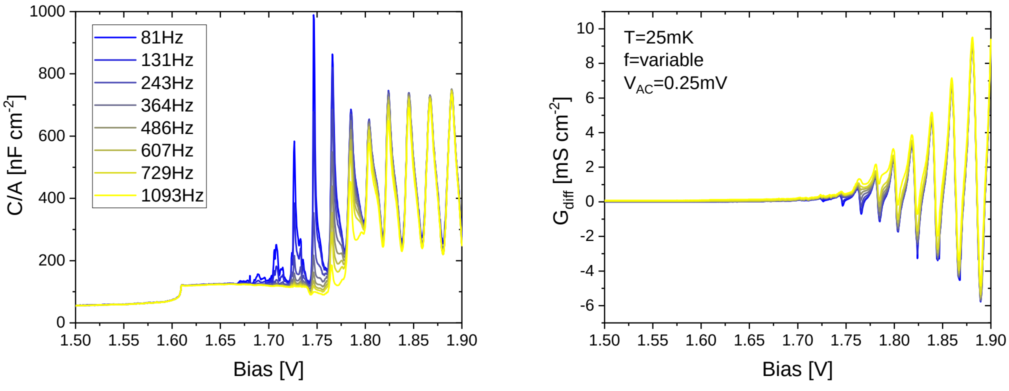

(a) C at different frequencies.

(b) G_{diff} at different frequencies.

Figure 5.6: Measurement series of a sample with a 10 nm thick barrier and a 90 nm wide QW. Temperature and AC amplitude were kept constant for all different frequencies. Figures adapted from [15].

5.3.3 Change of Quantum Well Width

This section discusses the main parameter that affects the oscillation period. A new series of wafers with varying quantum well width w was grown. The samples in this experiment had a 10 nm thick barrier and a single quantum well structure, shown in figure 5.7.

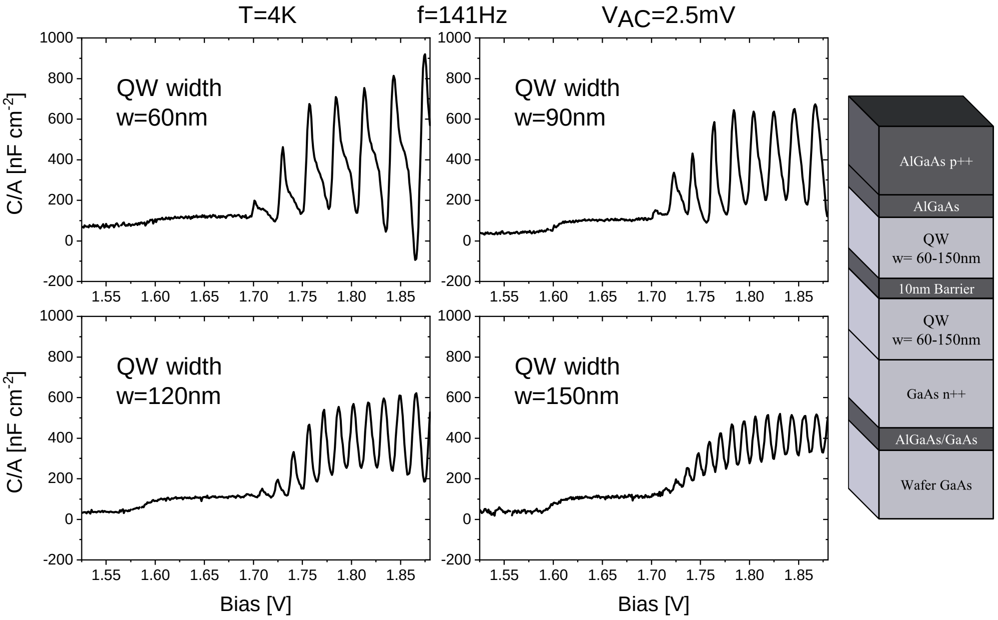

Figure 5.7: Measurement series of samples with different quantum well widths. The period of the oscillation decreases with increasing well width. The structure can be seen on the right side. Figure adapted from [15].

Varying the well width changed the peak-to-peak distance, as shown in figure 5.7. The oscillation period increases with decreasing well width. In order to extract the period value, the bias position of the peaks versus an assigned number (first peak has number 1, second peak number 2, etc.) was plotted. The slope of a linear fit to the data reveals the experimental period of the device. Figure 5.8(a) shows the result of this procedure. The graph also confirms that the peaks are equally spaced. Figure 5.8(b) shows that the period is proportional to $1/w$ and can be numerically described with $\Delta V = 1.603(30)\,\mathrm{V/w[nm]}$.

QW (nm)	Exp. Period (mV)	Theo. Period (mV)
60	29.4±0.3	34.9±0.4
90	20.4±0.2	25.7±0.4
120	15.6±0.1	19.6±0.2
150	12.2±0.1	16.3±0.2

Table 5.1: Data of four samples with different quantum well widths. The oscillation period decreases with increasing well width. Theoretical values are obtained from simulation.

Simulations with the different quantum well widths show the same linear behaviour in the relevant voltage range. The theoretical periods can be found together with the experimental ones in table 5.1. The theoretical values are in good agreement with the experimental ones, but they are up to 30% larger than the measured periods.

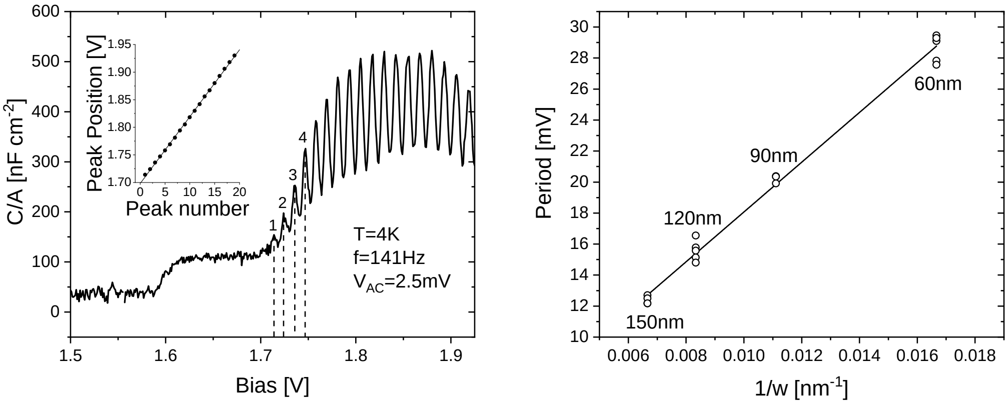

(a) Graph for illustration of the analysis method.

(b) Period as a function of QW width w. Different points denote different devices.

Figure 5.8: (a) Illustration of the data treatment, explained at an example device, with a 150 nm wide QW. Starting from the left, each peak was assigned its position number. The inset shows the peak position as a function of these peak numbers. The period can be calculated with a linear fit to the data points in the inset. (b) Periods of different samples scale linearly as a function of the inverse QW width. It can be seen that devices with the same well width have little variation.

5.3.4 Capacitance Oscillation Amplitude

In addition to the equal spacing of the capacitance peaks, another feature can be observed in the measurements. Their amplitude also scales inversely with the well width. Furthermore, the peaks exceed the expected geometrical value of $C_{\text{geo}} \approx 480\,\text{nF/cm}^2$, for the 2D charge systems being close to the barrier.

It can be seen in figure 5.3 that the capacitance peaks have their highest value at $C_{\text{max}} \approx 750\,\text{nF/cm}^2$. This is more than a factor of 1.5 times larger than the geometrical capacitance. This feature can be seen in all other samples as well, shown in figure 5.9. However, the difference between C_{max} and C_{geo} gets smaller with increasing well width. This finding is consistent with the second observation, the damping of the peaks. Figure 5.9 also shows that the height of the peaks (difference between maximum and minimum) also decreases with increasing well width. The peak height was determined for three arbitrarily chosen voltages. The results are written in table 5.2. Figure 5.9(b) shows, that G_{diff} evolves in a similar way.

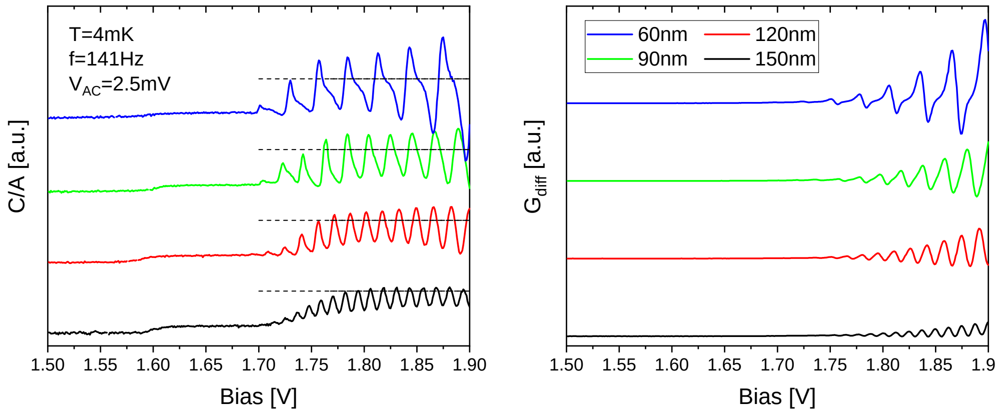

(a) Capacitance **(b)** Differential conductance

Figure 5.9: Measurements of samples with a 10 nm thick barrier and different well widths. The sample shown in this plot have a single quantum well structure (n-doping in GaAs). For clearer visibility of the effect, the lines are offset. Furthermore, the geometrical capacitance was added to graph (a) as a dashed line.

There is no clear reason why resonant tunnelling should lead to an enhanced capacitance. The device capacitance should be defined by the geometrical and quantum capacitance. C_{geo} is defined by the distance between the majority carriers on the two sides of the barrier. Simulations with *Nextnano* show that the average distance between the two 2DESs at the barrier is $d \approx 22\,\text{nm}$ (for a 10 nm-barrier), leading to $C_{\text{geo}} \approx 480\,\text{nF/cm}^2$. A capacitance value which is approached with an applied parallel magnetic field (section 5.3.7).

Unless the density of states is negative, the quantum capacitance can not enhance C either. Such a negative DOS has been used in theory to explain unusually large capacitances [38, 39].

It can be speculated that the electrons, tunnelling into the high index levels of the quantum well, have a slow recombination or relaxation rate, slower than the tunnelling lifetime. Therefore, the electrons would have an energy which is close to the one of the level on the n-side. Hence, they might tunnel back rather than relax to the bottom of the quantum well or recombine with a hole. This would reduce the effective distance between electrons and holes in the QW, resulting in the C peaks [15].

QW [nm]	$\Delta C(1.75\,\mathrm{V})$ [nF/cm^2]	$\Delta C(1.8\,\mathrm{V})$ [nF/cm^2]	$\Delta C(1.85\,\mathrm{V})$ [nF/cm^2]	$C_{\mathrm{max}}/C_{\mathrm{geo}}^{10}$
60	535	710	910	1.92
90	465	435	470	1.52
120	280	315	390	1.30
150	110	225	200	1.09

Table 5.2: To determine the height of a single peak, we took its maximum and subtracted the adjacent minimum on the right side (higher voltage). The data clearly shows, that the peak height decreases with increasing well width.

5.3.5 Low Bias Plateau

Another oddity of the measurement can be observed between 1.6 V and 1.7 V, the low bias regime. Here a C plateau has already developed, but the oscillations have not formed yet. Figure 5.10(a) shows the capacitance of two devices with a 10 nm thick barrier. One is a single quantum well structure (red line), and the other is a zero quantum well structure (black line), a sketch of the wafer structures is drawn in the inset. It can be seen that the zero QW device approaches the theoretical value of $C_{\mathrm{geo}}^{10} \approx 480\,\mathrm{nF/cm^2}$, which is expected for electron and hole layers being close to the barrier. On the other hand the single QW device (red line) saturates at lower value of $C_{\mathrm{p}} \approx 110\,\mathrm{nF/cm^2}$.

A trivial explanation would be that the 2D charge layers have not formed at the barrier yet. However, the results from the zero QW devices with either a 20 nm (section 4.2) or 10 nm (shown in figure 5.10(a)) thick barrier suggest that the two 2D layers have formed close to the barrier. They both approach their specific theoretical value of C_{geo} in the measurements.

Furthermore, simulations showed that the charge layers should have formed at the barrier, 5.10(b). The structure used in the simulation is a single quantum well structure with a 10 nm-barrier. The simulated distance between the electron and hole gas is about 22 nm, which is larger than the barrier width due to the broadening of the electron/hole wave function. From these results a geometrical capacitance of $C_{\text{geo}}^{10} \approx 480\,\text{nF}/\text{cm}^2$ is expected.

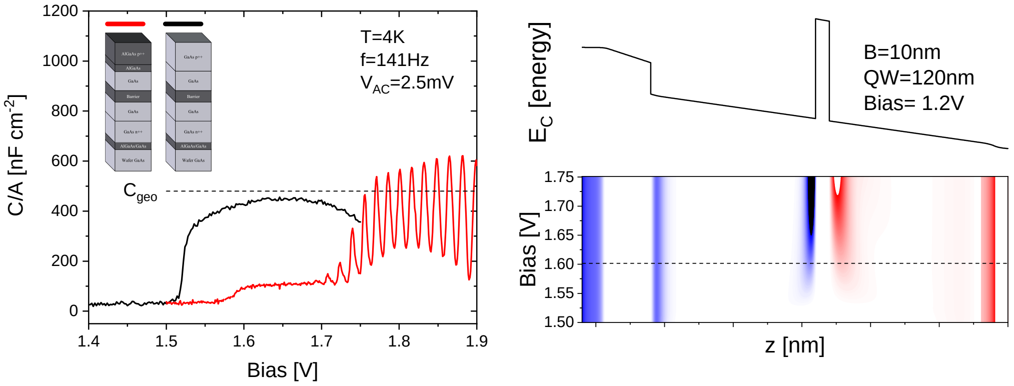

(a) Capacitance **(b)** Simulation of structure

Figure 5.10: (a) Measurements of samples with a 10 nm thick barrier and a well width of 120 nm. The samples with at least on quantum well (blue and red line) are almost identical. Whereas the sample without any quantum well (black line) does not show oscillations. However, its capacitance comes close to C_{geo}. (b) Simulation of the structure measured on the right side (red curve). The carrier density is shown as a function of position and bias, the holes drawn in blue colours and the electrons in red colours.

The origin of this phenomenon is not fully clear. The trivial explanation would be that the charge carriers have not accumulated at the barrier yet. However, experimental results and simulations support the opposite picture. The plateau forms at bias values before the RT-oscillations are observed. Therefore, it might be that it is not even connected to this model. Its origin remains unclear but may hint toward many-particle phenomena like a BEC of excitons or an excitonic crystal which would be expected to form in a low-density regime [40].

5.3.6 Temperature Dependence

The observed oscillations are rather robust and can be observed up to temperatures of 80 K, shown in figure 5.11. For a better visibility, the measurements are presented in two different data sets. Figures 5.11(a) and (b) show the data measured in our ^{3}He evaporation system (see section 3.4.3). In this system, the temperature could be set in the range from 250 mK up to 1.4 K. No changes in C or G_{diff} were observed within this temperature range.

The second temperature range was measured in our dewar setup. In order to reach temperatures above 4 K a heater was used, in combination with manually adjusting the distance between the liquid helium and sample. Figures 5.11(c) and (d) show the capacitance and differential conductance for the high temperature range. The oscillations are clearly visible up to 70 K. At 80 K the oscillations vanish in capacitance but are still faintly visible in G_{diff}. Due to their increased thermal energy, electrons can overcome the barrier at a lower bias. This results in lower breakdown voltages, as shown in figure 5.11(d). Furthermore, the peaks shift in position. This behaviour is contributed to the change of the band gap energy with temperature. However, the oscillation period is almost constant over the whole temperature range, as seen in table 5.3.

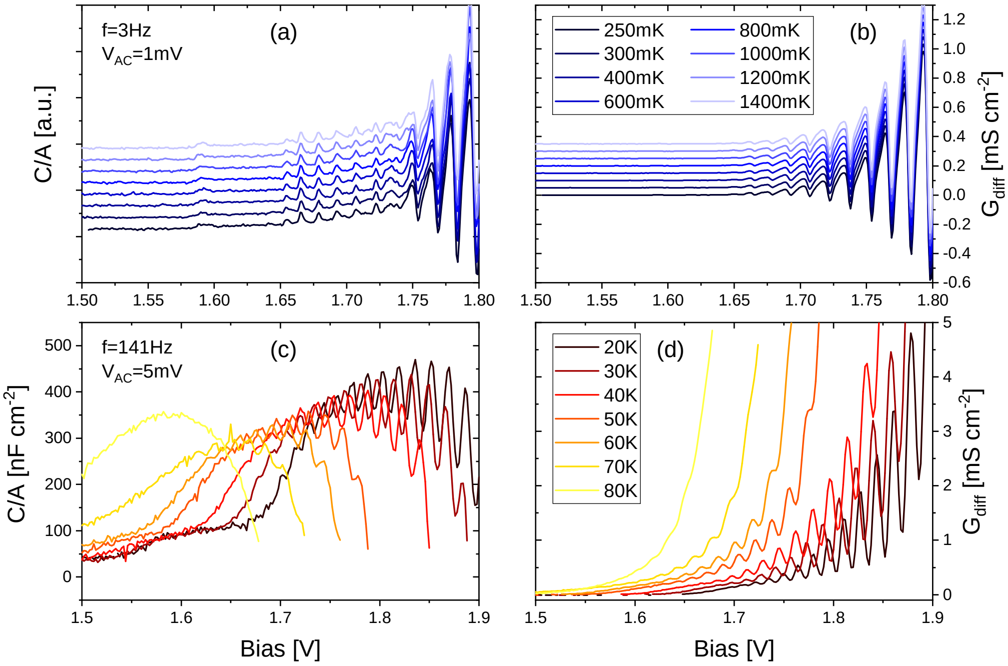

Figure 5.11: Bias sweeps at different temperatures of a sample with a 10 nm thick barrier and a 120 nm wide quantum well. The data from graphs (a) and (b) were measured in the ^{3}He evaporation system. In order to distinguish between the individual temperatures, an arbitrarily chosen offset is added to each line. (c) and (d) were measured in the dewar setup. The temperature was set with a heater, and adjusting the distance between liquid He and the sample. This was done by lifting the sample rod. The height of the sample rod was constantly adjusted to ensure a temperature fluctuation of less than 1 K.

It can be concluded that temperature has almost no influence on the oscillation period. Higher temperatures change the appearance of the oscillations, but this is due to the thermal change of the band gap and the fact that the electrons are more likely to shoot over the barrier.

5.3.7 Magneto-Capacitance

The influence of a magnetic field on the samples, which did not show resonant tunnelling, has already been discussed. This section presents the behaviour of the RT-oscillations in an applied magnetic field. The two devices measured have both a single quantum well structure with a 10 nm-barrier and either a 120 nm or a 90 nm wide QW. It is not expected that the different well width changes the behaviour in a magnetic field.

T (mK)	Experimental Period (mV)	T (K)	Experimental Period (mV)
250	14.55±0.18	20	15.65±0.23
300	14.55±0.18	30	16.21±0.20
400	14.57±0.19	40	16.64±0.17
600	14.62±0.17	50	16.07±0.28
800	14.65±0.17	60	16.29±0.16
1000	14.55±0.18	70	17.70±0.48
1200	14.61±0.19	80	17.40±0.89
1400	14.65±0.17	-	-

Table 5.3: Period calculated from the measurements shown in figure 5.11. The left side shows very little changes with temperature. On the right side a small increase of the period with rising temperature can be observed. Due to the small number of peaks at the highest temperatures (70 and 80 K) their error is bigger compared to other temperatures.

In a first experiment, a perpendicular magnetic field was applied. Figure 5.12(a) shows the measured capacitance as a function of bias and magnetic field strength. Landau levels are only faintly visible between 1.6 and 1.725 V. Figure 5.12(b) shows two cuts of the colour plot at 0 and 2 T. The measurements suggest that a perpendicular B-field barely affects the oscillations.

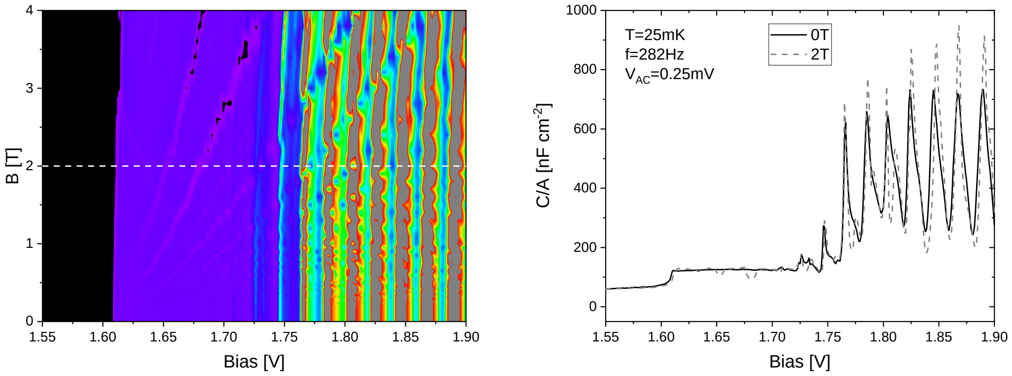

(a) C as a function of bias and magnetic field. **(b)** Two horizontal line cuts at $B = 0$ and 2 T.

Figure 5.12: Capacitance in an applied perpendicular magnetic field of a 10 nm-barrier device with a 90 nm wide quantum well. Faint traces of a Landau fan can be observed. Figures adapted from [15].

By applying an in-plane (or parallel) magnetic field, a drastic effect on the oscillations, in contrast to the perpendicular field, was observed. Figure 5.13(a) shows the same measurement as figure 5.12(a), but the sample was tilted by 90°. It can be seen that at 0.5 T the amplitude of the oscillations starts to decrease. In figure 5.13(b) two cuts at 0 and 2 T, from the colour plot are shown. These figures show a complete suppression of the oscillations above 2 T. Furthermore, the capacitance saturates at a second plateau. This new level is close to the expected geometrical value of 480 nF/cm^2 for charges directly at the barrier.

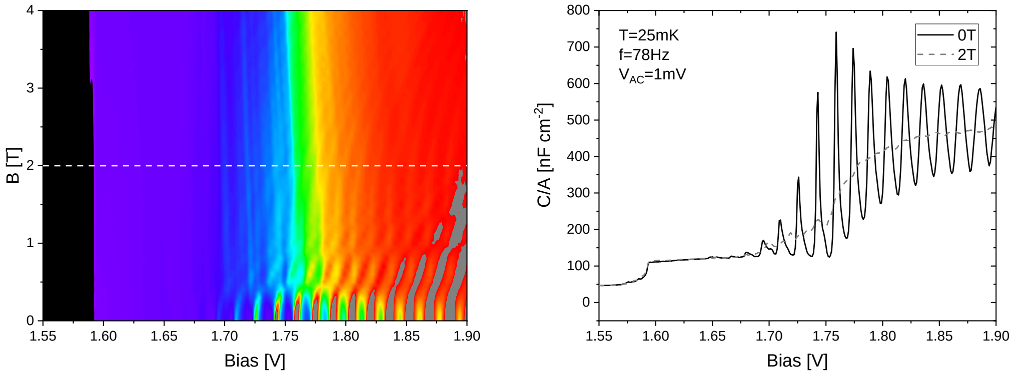

(a) C as a function of bias and magnetic field. **(b)** Two horizontal line cuts at $B = 0$ and 2 T.

Figure 5.13: Capacitance in a parallel magnetic field of a 10 nm-barrier device with a 120 nm wide quantum well. A complete suppression of the oscillations is observed above 2 T. Figures adapted from [15].

These results support the resonant tunnelling model. The perpendicular magnetic field (figure 5.12) causes Landau quantisation on both sides of the barrier, which does not affect tunnelling much. Therefore, it is possible for electrons to tunnel at similar voltages as in zero magnetic field. The experiment indeed shows that the oscillations are hardly disturbed by a perpendicular B-field.

In contrast, a parallel field reduces tunnelling, as the in-plane momentum is no longer conserved. In the experiment (figure 5.13), a damping of the oscillations with a parallel B-field is observed. The RT-oscillation experience a complete suppression above 2 T.

5.4 Double Quantum Well Structure

The section before focused on results from devices with a single QW structure, i.e. the p-doping was placed in AlGaAs and the n-doping in GaAs. In this section, the role of an n-side quantum well is studied. Therefore, both dopings were placed in AlGaAs, leading to a double quantum well structure. The quantum wells were grown with the same width on both sides of the barrier. The thickness of the barrier remained unchanged at 10 nm.

Figure 5.14 compares the single QW and the double QW structure. Both devices share the same quantum well width of 120 nm. Therefore they only differ in the doping layout, shown in the inset in 5.14(a). As seen in figure 5.14, there is hardly any difference between the two samples, neither in capacitance nor differential conductance.

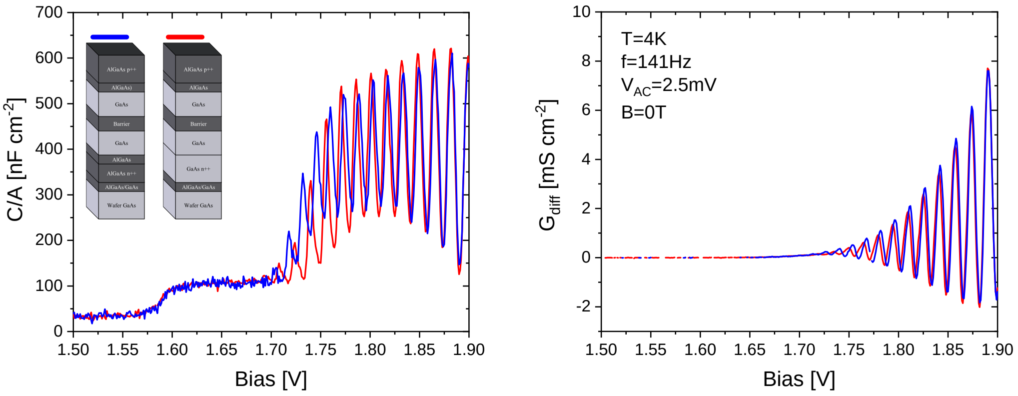

(a) Capacitance **(b)** Differential conductance

Figure 5.14: Both samples used in this graph have a 10 nm thick barrier and their quantum wells are 120 nm wide. The only difference (as can be seen in the inset in (a)) is, that the n-doping was placed in GaAs (red line) or in AlGaAs (blue line). The measurements show, that there is no notable difference between the two structures, neither in C nor in G_{diff}.

In order to further examine the influence of the second quantum well on the RT-oscillations, some experimental series from the single QW sample were repeated with this new double QW structure. Please be reminded that all following measurements were carried out on samples with the double QW structure and a 10 nm-barrier.

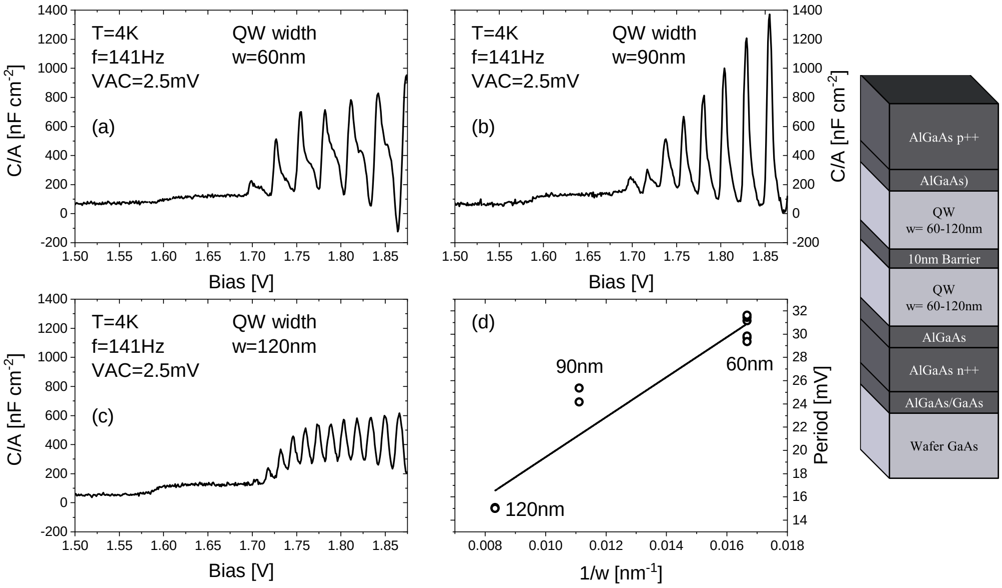

Figure 5.15: (a)-(c) Capacitance for different quantum well widths. The period of the oscillation decreases with increasing well width. The structure can be seen on the right side. (d) Periods of different samples as a function of the inverse quantum well width. The devices with the same well width have little variation.

Figure 5.15 shows measurements of devices with different quantum well widths, ranging from 60 nm up to 120 nm. It can be seen that the oscillation period decreases with increasing well width. The measured and theoretical oscillation periods are summarised in table 5.4.

Comparing the results of this structure type (double QW) with the ones of single QW devices shows that the periods of the same QW width are quite similar for both structure types. The ratio between the well width and the period is also shown in graph 5.15(d) and its numerical value is 1.720(160) V/w[nm], which is close to 1.603 V/w[nm] of the single quantum well devices.

The magnetic field experiment was also repeated with the double QW device. The results for a perpendicular field are shown in figure 5.16. Both devices behave similarly. In the bias range from 1.6 V to 1.7 V, faint Landau levels can be observed, as in the single QW device, figure 5.13(a). The RT-oscillations are again barely affected by the magnetic field. In summary, the double QW structure behaves similarly in a perpendicular magnetic field as the single QW structure.

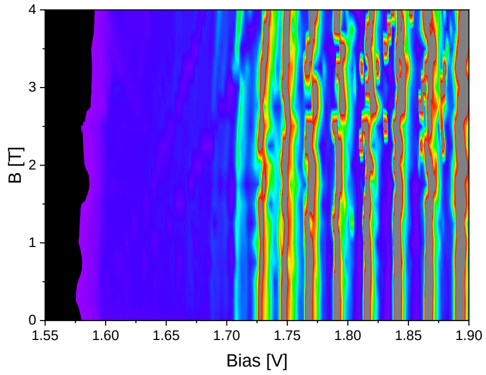

Figure 5.16: Capacitance as function of bias and magnetic field. The devices has 90 nm wide quantum wells. The measurement was taken at a base temperature of 25 mK, $f = 78\,\text{Hz}$ and $V_{AC} = 1\,\text{mV}$. Faint Landau level formation is visible below 1.7 V. The oscillations are almost undisturbed by the applied magnetic field.

QW (nm)	Exp. Period (mV)	Theo. Period (mV)
60	29.5±0.3	36.8±1.1
90	25.4±0.4	27.5±0.5
120	14.9±0.2	20.6±0.3

Table 5.4: Data of three samples with different quantum well widths and a 10 nm-barrier. The oscillation period decreases with increasing well width. Theoretical values are obtained from simulations.

5.4.1 Electro Luminescence

The double QW structure was used in electro luminescence (EL) measurements (there are no corresponding measurements for the single QW structure). In this experiment, the energy of the photons emitted by the device is recorded.[2]

---

[2] This experiment was done in collaboration with Dr. Mirko Lupatini, who carried out the measurement and supported the analysis of the data.

EL is observed at 1.515 eV only. That is the energy expected for the recombination of electrons from the bottom of the conduction band with holes from the top of the valence band. The lack of EL signal at higher photon energies implies that electrons, which tunnelled into the high index subband, do not recombine directly with the holes.

Figure 5.17(b) shows the IV characteristics of the device (black solid line) and a horizontal cut of the electro luminescence at 1.515 eV. It can be seen that the oscillations of the current coincide with the oscillations in luminescence.

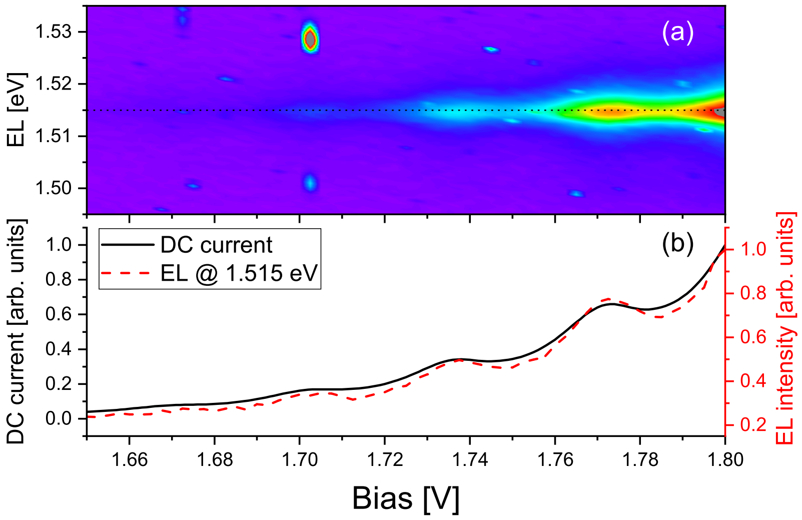

Figure 5.17: (a) Electro luminescence measurement of a device with a 10 nm thick barrier and a 60 nm wide quantum well. The EL shows oscillations which match with the oscillations in the current. The EL intensity was rather weak. Therefore, a high sensitivity was used, what lead to spurious signals (e.g. at 1.53 eV. (b) EL at its maximal intensity (1.515 eV) shows the same oscillations as the current across the device. The data was measured by Dr. Mirko Lupatini. Figure from [15].

Similar experiments were done for the double QW structure as for the single QW one. The results of the measurements show no noteworthy differences between the two structure types. This leads to the conclusion that it makes no difference (for the RT-oscillations) if the n-doping is placed in GaAs (single QW) or AlGaAs (double QW). The reason why a QW on the n-doped side of the barrier does not lead to any particularities could be the large mass of the holes. This makes any tunnelling (resonant or not) into a QW on the n-side very unlikely.

Most of the experiments presented in this chapter support the idea of resonant electron tunnelling into high index energy levels to be the origin of the newly observed oscillations. However, there are also features of the measurements which cannot be explained in the single particle picture of resonant tunnelling. This does not disprove the model, but there is still more research needed to be able to fully understand the newly observed phenomenon.

Chapter 6

Preliminary Results

Measurements which were not yet analysed thoroughly are presented in this chapter. The first part deals with additional data on the device with a 10 nm wide barrier and both dopings placed in GaAs (zero quantum well structure). This device was already discussed in section 5.1, but another feature is presented here. The chapter continues with measurements on devices with weak tunnelling (i.e. a 15 nm thick barrier), which have not been shown before.

6.1 Capacitance Anomaly at Threshold Voltage

In section 5.1 data of a zero quantum well device with a 10 nm were shown. Here, a feature of these measurements which has not been discussed yet is presented. It can be also seen in both samples with the 20 nm barrier. Figure 6.1 shows the measurements of these three heterostructures:

- 20 nm thick barrier, zero quantum well structure, figure 6.1(a)
- 20 nm thick barrier, double quantum well structure, figure 6.1(b)
- 10 nm thick barrier, zero quantum well structure, figure 6.1(c)

In the bias region directly after the onset of the capacitance plateau, a peak or overshoot can be observed. While the measurement of the 20 nm barrier devices (figures 6.1(a) and (b)) do only suggest the presence of the peak, it can be clearly identified in the measurement of the 10 nm-barrier device (figure 6.1(c)). This peak is only observed in these three heterostructures and at temperatures below 4 K.

This peak does not develop in devices with a 10 nm-barrier, which show the RT-oscillations. A striking difference between these two groups of devices (RT-oscillation vs C anomaly at V_{th}) is the height of the capacitance plateau. The RT-oscillation devices saturate at the low value presented in section 5.3.5. In contrast, the devices developing the anomaly approach their geometrical value.

The theoretical geometrical value is calculated for the two charge layers close to the barrier.

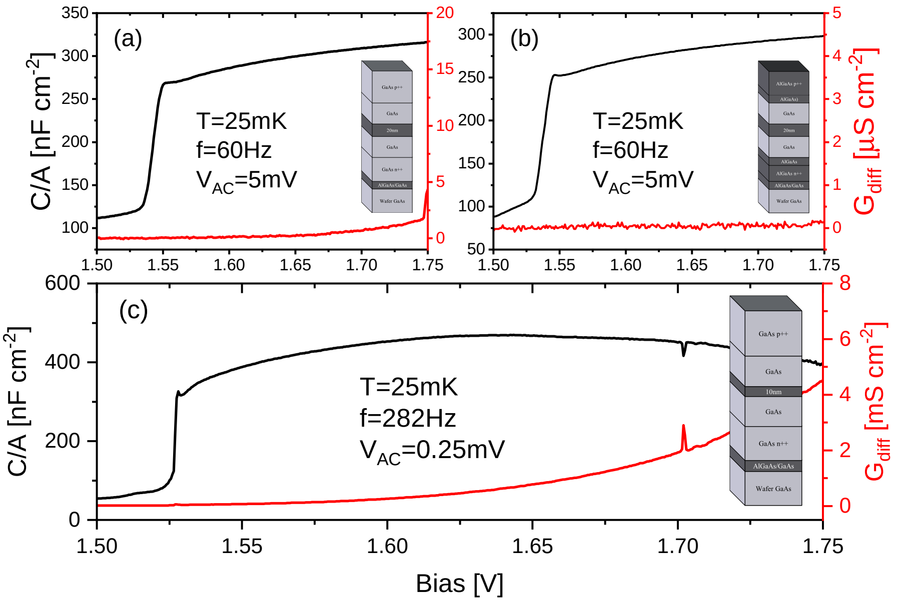

Figure 6.1: (a) and (b) Measurements of devices with a 20 nm thick barrier. The anomaly in capacitance can be see at 1.55 V. (c) Measurement of a zero quantum well device with a 10 nm thick barrier. The overshoot can be seen at 1.525 V.

This leads to the assumption that the effect which reduces the capacitance value and forms the low C plateau also hinders the development of the anomaly at the threshold bias. Another observation from figure 6.1 is that the reduction of the barrier thickness increases the peak height ((a) and (b) 20 nm-barrier, (c) 10 nm-barrier). This can be interpreted as follows: the peak is related to the interaction strength of the 2DEG and 2DHG.

Figure 6.2(a) shows an enlargement of the relevant bias region. The measurement was carried out using the same device as already used in figure 6.1(c), a zero QW structure with a 10 nm-barrier. Additionally, a magnetic field was applied, and the frequency of the AC voltage was varied. Figure 6.2(a) shows a zoom-in on the anomaly, figure 6.2(b) shows the measurements with applied magnetic field and varied frequency. The formation of Landau levels can be seen in fig. 6.2(b). At low magnetic fields, the peak is still visible. However, with increasing field strength, the Landau levels start to cover the peak. Furthermore, the peak is not influenced by the changing frequencies.

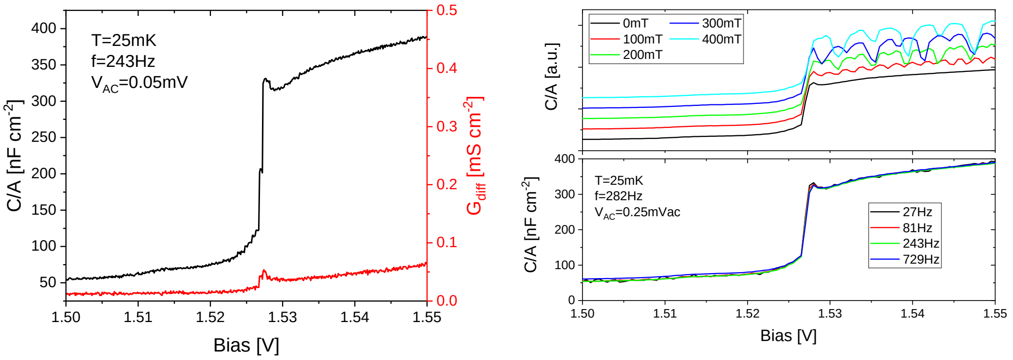

(a) C and G_{diff} with higher resolution. **(b)** C as function of B-field and frequency.

Figure 6.2: (a) Higher resolution measurement of the overshoot at capacitance step. G_{diff} shows a peak in the same bias region as well. (b) Top: Measurement series at different magnetic fields. Landau level formation can be observed already at 100 mT. With increasing field strength, the magnetic effects start to cover the anomaly. Bottom: Measurements at different frequencies show, that the peak does not depend on f.

This unexpected peak in C was also observed and described by Dr. Michael Pohlt in his doctoral thesis [36]. He concluded that this peak could be described by a combination of interaction and geometrical effects, which correspond to an excitonic correlation. This picture is in good agreement with the work done by G.W. Burg et al. in 2018 [13]. They observe strongly enhanced tunnelling between two graphene sheets, separated by a barrier, at charge neutrality. This could point towards the formation of a many-body state with electron-hole pair condensation. In our device, we also observe an increase in tunnelling current at the onset of the capacitance plateau, figure 6.2(a). A condensation of electron-hole pairs would be expected at low carrier densities. It is assumed that the charge systems measured for this thesis have a low carrier density at low bias. This suggests that the C anomaly could be related to such a condensation. However, this topic still needs more research to confirm such an assumption.

6.2 Experimental Results on intermediate interacting 2DESs (15 nm-Barrier)

This section presents measurements of a structure which has not been discussed yet. The new devices have a 15 nm thick barrier and either a single or double quantum well structure.

6.2.1 Capacitance and Hysteresis Effect

Figure 6.3 shows the data of a device with 15 nm-barrier sample. At first glance, the device behaves as a sample with a 20 nm thick barrier. The capacitance increases as the 2DESs form close to the barrier, and no peaks due to resonant tunnelling are observed. However, a closer look at the capacitance reveals that the plateau is not at the expected height of $C_{\mathrm{geo}}^{15} \approx 390\,\mathrm{nF/cm^2}$ (for the charge layers having formed close to the barrier). Instead, C reaches the same value as the plateau of the samples with a 10 nm barrier $C_{\mathrm{p}}^{10} \approx 110\,\mathrm{nF/cm^2}$. Furthermore, two peaks close to 1.9 V appear, which seem unrelated to resonant tunnelling.

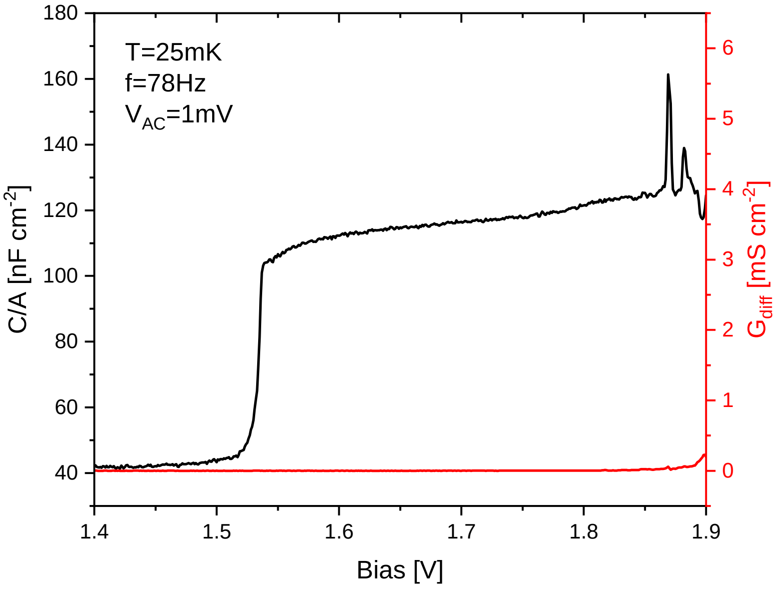

Figure 6.3: Capacitance and differential conductance of a device with a 15 nm thick barrier a 120 nm wide single quantum well. C shows the step like increases, as the devices with different barrier thickness. The plateau reaches the same value as the low bias plateau discussed in section 5.3.5. No tunnelling up to almost 1.9 V is observed.

The direction of the bias sweep was not important for the 10 or 20 nm-barrier devices. However, the 15 nm-barrier capacitor shows an apparent hysteresis effect.

Figure 6.4 shows the up and down sweep for a 15 nm-barrier device. A time-resolved measurement is displayed in the inset. In order to record this data, a regular bias sweep was done. But instead of going back to zero bias, the down sweep was stopped at 1.515 V (red point in figure 6.4). This voltage was chosen since the difference between the two sweep directions is maximal at that point. Fitting an exponential decay[1] to the curve in the inset, results in a lifetime of $\tau = 4.52\,\mathrm{min} \pm 0.06\,\mathrm{min}$ at 250 mK.

Another feature of the hysteresis can also be seen in figure 6.4. The structures at high bias (above 1.8 V) do not show any hysteresis. This leads to the assumption that the effect only occurs at low or intermediate density.

---

[1] The formula used for the fit is $C(t) = C_0 + C_1 \exp(-t/\tau)$

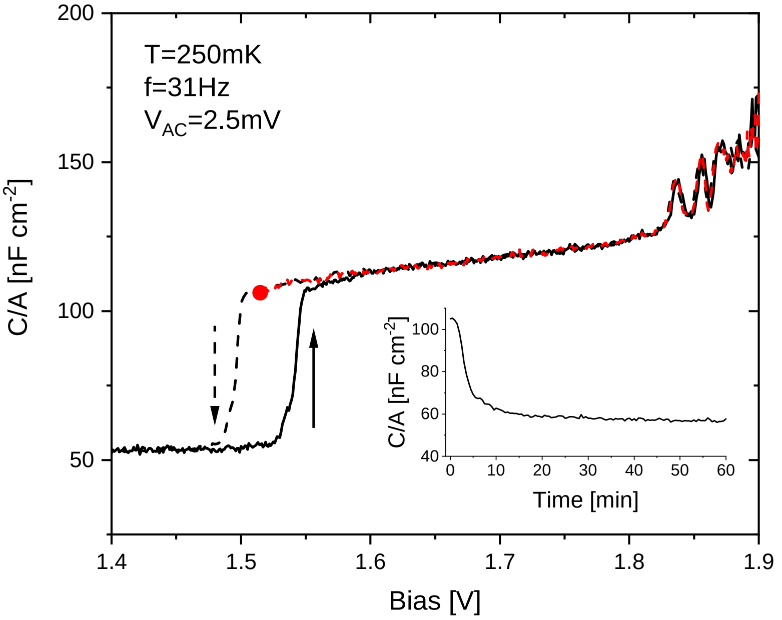

Figure 6.4: Bias sweeps in both directions. The hysteresis effect can be identified by the different threshold voltages. The red line depicts the second down sweep, which was stopped at the red point, for the time-resolved measurement shown in the inset. The devices used had a double quantum well structure with a 15 nm thick barrier and 90 nm wide QWs.

6.2.2 Recovery of Resonant Tunnelling

Resonant tunnelling oscillations could be recovered on a device with a 15 nm-barrier. This was done by taking a sample piece from the outer region of the wafer. The MBE growth rates are not the same over the whole wafer. The systems are calibrated on the wafer centre. The rates decrease towards the wafer edge[2], resulting in thinner layers. With this thinner barrier, the electrons are more likely to tunnel through it, and the resonant tunnelling peaks are observed again.

This is depicted in figure 6.5. Both samples were cleaved from the same wafer but different positions. The red curve is measured on a centre piece, whereas the blue curve is measured on an edge piece. The centre piece does not show any RT-oscillations, but it does show the hysteresis effect. In contrast, the edge device (blue curve) does not experience any hysteresis between the up (solid blue line) and the down (dashed blue line) sweeping direction. However, the RT-oscillations can be seen. The wafer from which the two devices were fabricated has a single QW structure with a 120 nm wide well and a 15 nm thick barrier.

---

[2] More information on this topic can be found in the thesis of Dr. Christian Reichl [19].

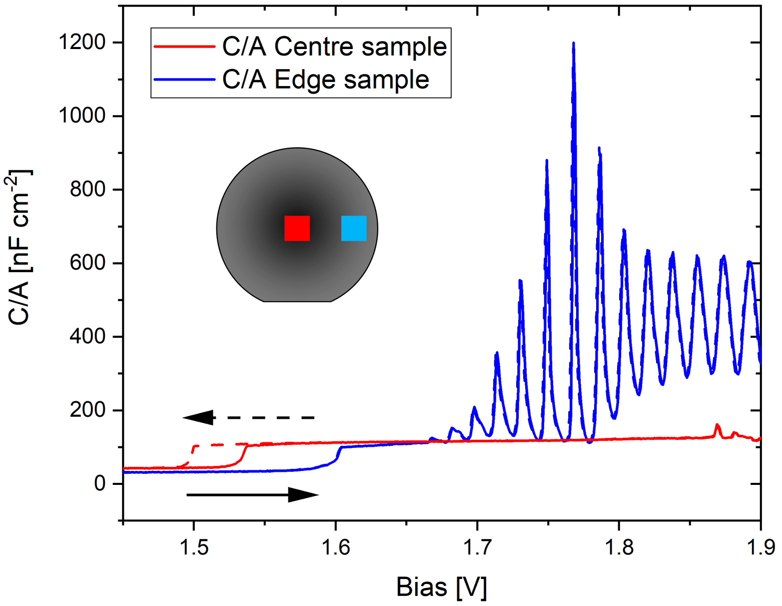

Figure 6.5: Comparison between a centre piece (red line) and a edge sample (blue line). The centre piece behaves as a regular device with a 15 nm thick barrier. The hysteresis effect can be seen as well. On the other hand, the edge sample shows capacitance peaks which can be related to resonant tunnelling.

The period of the oscillation is 17.4(1) mV. This is larger than the corresponding period of the 10 nm device, 15.6(1) mV from table 5.1. This is consistent with the reduced growth towards the wafer edge. Due to the lower rate, the QWs of the edge sample are a bit smaller than 120 nm, which results in a larger oscillation period.

6.2.3 Magneto-Capacitance

Experiments in a (perpendicular) magnetic field were carried out as well. The used device had a single QW structure with a 120 nm wide well and a 15 nm-barrier. Similar to the measurements of devices with a 10 and 20 nm thick barrier, capacitance minima due to the altered density of states were observed. Figures 6.6(a)-(c) show a series of measurements at different B-field strengths. Due to the hysteresis, both sweeping directions, up and down, are plotted.

The behaviour of the hysteresis mentioned before can now be seen distinctly. Above a bias of ≈ 1.725 V the hysteresis effect vanishes. Furthermore, in figure 6.6(a), it can be seen that the distance between adjacent minima increases below 1.725 V. A potential interpretation is that the carrier density does change its bias dependence at this particular voltage. Figure 6.6(d) supports this picture, since the slope changes at 1.75 V. Above this voltage, the system needs more bias to change its density.

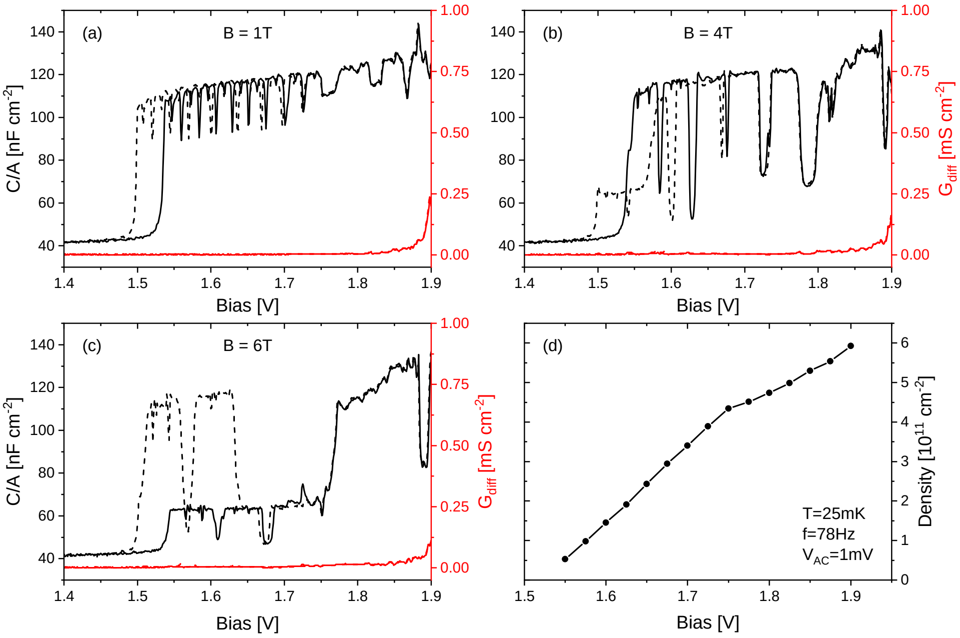

Figure 6.6: (a)-(c) Capacitance and differential conductance at different magnetic fields as a function of bias. Both sweeping directions are plotted, up (solid lines) and down (dashed lines). (d) Carrier density as a function of bias. The slope of the density-bias relation changes at 1.75 V.

Another observation which can be made in figure 6.6(b) and (c) is the formation of an intermediate-level at ≈ 60 nF/cm^2. The occurrence of this intermediate-level seems arbitrary, especially by comparing the two sweep directions. However, combining the single measurements to a 2D colour map (figure 6.7) reveals that this new level does not occur randomly. The white arrows indicate the starting point of this feature. It can be seen twice in each sweep direction.

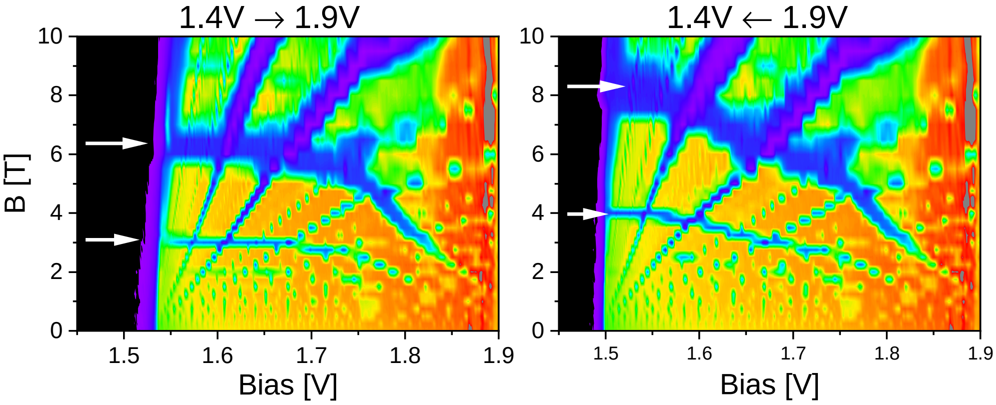

Figure 6.7: Capacitance as a function of magnetic field and bias. A Landau fan can be observed in both sweeping direction as well as the new phenomenon.

In these graphs, two different kinds of structures can be seen, the formation of the Landau levels and the resulting Landau fan, as well as the formation of the intermediate-level, which behaves opposite to the Landau level formation. The minima due to the Landau quantisation behave as theory predicts. But the newly observed structure develops towards a lower magnetic field with increasing bias (or density). It is assumed that both branches (upper and lower arrows) can be contributed to the same effect, as they behave similarly. This phenomenon is new to us and needs more research to understand it fully.

Chapter 7

Conclusion and Outlook

Capacitance of a p-i-n junction with different barriers was studied in this thesis. Even though the devices seem relatively simple, capacitance measurements have shown a non-trivial behaviour. Especially the thickness of the barrier plays a crucial role in the device performance, as it controls the interaction strength between the charge layers. Devices with three different barrier widths were studied, each showing distinct features.

It is expected that an applied forward bias to the p-i-n structure forces the charge carriers to accumulate on both sides of the barrier. Experiments and simulations, in chapter 4, confirm that the charge systems indeed form close to the barrier and also have a 2D character.

The second part followed with the characterisation of a zero quantum well device (both dopings placed in GaAs) containing a 10 nm-barrier. The results resemble the behaviour described above and support the conclusion of the formation of 2DESs on both sides of the barrier.

The work continues with studies of single and double quantum well structures (p-doping in AlGaAs, n-doping in GaAs or AlGaAs). The most striking feature of the measurements is the equally spaced peaks in capacitance and differential conductance. It was found that the effect is independent of the applied AC frequency (within the measuring range of $30 - 1000\,\mathrm{Hz}$) and can be observed up to 80 K. The oscillation period changes with the with of the quantum well. An in-plane magnetic field above 2 T completely suppresses the oscillations.

Resonant tunnelling of electrons into high index energy levels in the quantum well is proposed as a model. The experimental results fit this model and the presented simulations.

The large and oscillating capacitance could indicate that the electrons in the quantum well do not recombine but remain in equilibrium with the n-contact. Thus, electrons and holes would coexist in the QW. Capacitance would then depend on the relative position of the electrons and holes and their interaction.

Making quantitative estimates was not feasible, as there is no theory available that would describe the behaviour of such a charge carrier gas.

The data acquired from the single and double quantum well structures did not show any significant differences. Both devices develop the C and G_{diff} peaks, which can be attributed to resonant tunnelling. Even the oscillation period scales with the inverse quantum well width in both structures. Therefore, it can be assumed that the quantum well on the p-side of the barrier is relevant for resonant tunnelling.

Furthermore, preliminary data of samples with a 15 nm-barrier were presented. The features discussed in this thesis are listed below and shown in figure 7.1.

- (1) Capacitance peaks exceeding C_{geo}
- (2) Low capacitance plateau at small bias
- (3) Capacitance overshoot in the zero quantum well sample
- (4) Hysteresis effect of the 15 nm-barrier device
- (5) New structure in a magnetic field

These features are new and potentially very interesting, as they hint towards the appearance of many-body effects, e.g. a BEC. However, they cannot be fully explained within a single particle picture.

In this thesis, a p-i-n junction containing a barrier and quantum wells was used to confine electrons and holes at the barrier. Several new phenomena have been discovered which deserve further studies, focusing on the effects of the 10 nm-barrier device (points (1)-(3) in figure 7.1). Most interesting is the possibility of observing BEC, which is expected at a sufficiently small distance and low temperature.

Narrower quantum wells could squeeze the electronic wave functions and bring them closer to the barrier. Furthermore, the two 2DHG would eventually collapse into one system. This would result in the loss of equal spacing between the peaks. Another suggested experiment is lateral transport measurements, especially counterflow measurements. Such a study could give valuable insights into the physics of the electron-hole bilayer system. Furthermore, the capacitance overshot at the threshold voltage could be measured as a function of temperature, figure 7.1(b). This could yield a critical temperature related to the condensation of excitons.

The experiments suggested in the paragraph above can also be performed on the 15 nm-barrier device. Especially the new magnetic field structure (figure 7.1(d)) might uncover other interesting phenomena. Another starting point for further studies could be to measure the lifetime of the hysteresis effect as a function of temperature.

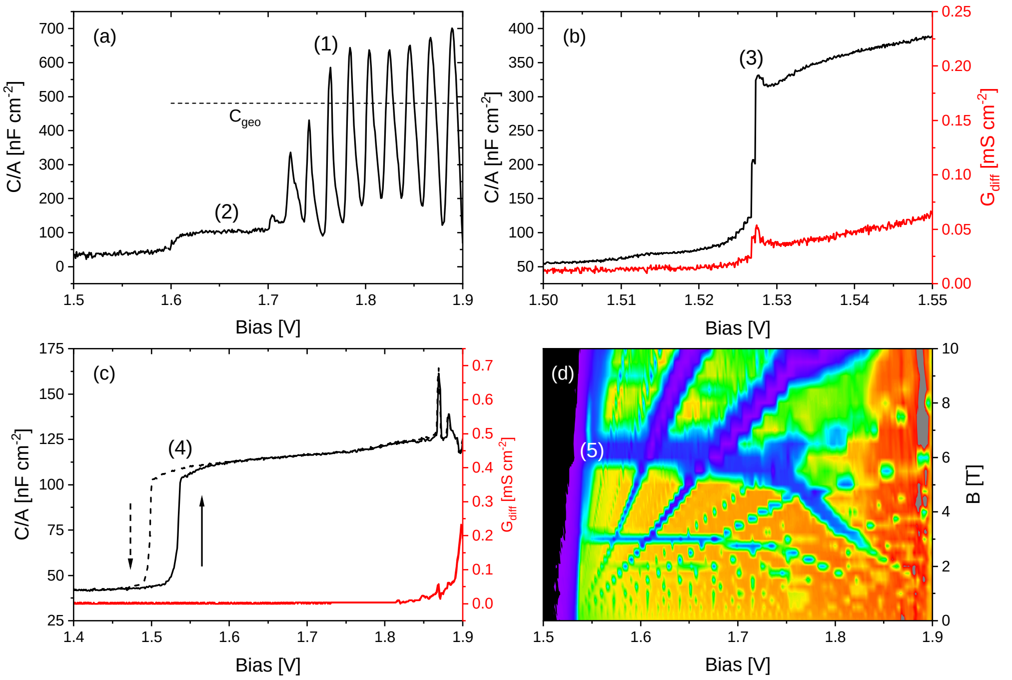

Figure 7.1: (a) Single quantum well sample with a 10 nm-barrier and 90 nm quantum well. (b) Zero quantum well sample with a 10 nm-barrier. (c) Single quantum well device with a 15 nm thick barrier and 120 nm quantum well. (d) Capacitance of a single quantum well sample with a 15 nm-barrier and a 120 nm quantum well, as a function of bias and magnetic field.

In summary, a system for the electrical generation of electron-hole bilayers was developed and improved. Capacitance oscillations in samples with a small barrier width were found. Resonant tunnelling of electrons into high index energy levels seems to be an appropriate model. Furthermore, effects which cannot be explained by this single particle picture were observed. In order to fully understand them, further research is needed.

Bibliography

[1] J. M. Blatt, K. W. Böer, and W. Brandt, Phys. Rev. **126**, 1691 (1962).

[2] D. Snoke, Science **298**, 1368 (2002).

[3] L. V. Butov, A. C. Gossard, and D. S. Chemla, Nature **418**, 751 (2002).

[4] M. Beian et al., EPL **119**, 37004 (2017).

[5] H. Deng, G. Weihs, C. Santori, J. Bloch, and Y. Yamamoto, Science **298**, 199 (2002).

[6] J. Kasprzak et al., Nature **443**, 409 (2006).

[7] Y. E. Lozovik and V. I. Yudson, Jetp Lett. **22**, 274 (1975).

[8] S. Shevchenko, Sov. J. Low Temp. Phys. **2**, 251 (1976).

[9] U. Sivan, P. M. Solomon, and H. Shtrikman, Phys. Rev. Lett. **68**, 1196 (1992).

[10] M. Pohlt et al., Appl. Phys. Lett. **80**, 2105 (2002).

[11] A. F. Croxall et al., Phys. Rev. Lett. **101**, 246801 (2008).

[12] J. A. Seamons, C. P. Morath, J. L. Reno, and M. P. Lilly, Phys. Rev. Lett. **102**, 026804 (2009).

[13] G. W. Burg et al., Phys. Rev. Lett. **120**, 177702 (2018).

[14] Z. Wang et al., Nature **574**, 76 (2019).

[15] S. Parolo et al., Phys. Rev. B **105**, 035304 (2022).

[16] M. Lupatini, *Polaron-polaritons and quantum Hall ferromagnetism in hole gases*, PhD thesis, ETH Zuricht, 2020.

[17] I. Vurgaftman, J. R. Meyer, and L. R. Ram-Mohan, Journal of Applied Physics **89**, 5815 (2001).

[18] T. Ihn, *Semiconductor Nanostructures: Quantum states and electronic transport*, Oxford University Press, 2010.

[19] C. Reichl, *MBE growth of ultrahigh-mobility 2DEGs in GaAs/AlGaAs*, PhD thesis, ETH Zurich, 2014.

[20] P. Harrison, *Quantum wells, wires, and dots: theoretical and computational physics*, Wiley, Chichester New York, 2003.

[21] J. Singh, *Electronic and Optoelectronic Properties of Semiconductor Structures*, Cambridge University Press, Cambridge, 2003.

[22] S. Adachi, *GaAs and Related Materials: Bulk Semiconducting and Superlattice Properties*, World Scientific Singapore, 1994.

[23] K. P. Loh, Nature Nanotechnology **12**, 837 (2017).

[24] J. E. Golub, K. Kash, J. P. Harbison, and L. T. Florez, Phys. Rev. B **41**, 8564 (1990).

[25] M. Bayer, V. Timofeev, F. Faller, T. Gutbrod, and A. Forchel, Phys. Rev. B **54**, 8799 (1996).

[26] R. Busch, *Elektrotechnik und Elektronik: Für Maschinenbauer und Verfahrenstechniker*, Springer Vieweg Wiesbaden, 2015.

[27] S. Luryi, Applied Physics Letters **52**, 501 (1988).

[28] T. Li et al., Nature Nanotechnology **16**, 1068 (2021).

[29] K. V. Klitzing, G. Dorda, and M. Pepper, Phys. Rev. Lett. **45**, 494 (1980).

[30] D. C. Tsui and A. C. Gossard, Applied Physics Letters **38**, 550 (1981).

[31] P. A. Tipler and G. Mosca, *Physik: für Wissenschaftler und Ingenieure*, Springer-Verlag Berlin Heidelberg, 2015.

[32] S. M. Sze and K. K. Ng, *Physics of Semiconductor Devices*, John Wiley & Sons, Inc., 1981.

[33] J. Faist et al., Science **264**, 553 (1994).

[34] J. P. Eisenstein, T. J. Gramila, L. N. Pfeiffer, and K. W. West, Phys. Rev. B **44**, 6511 (1991).

[35] S. Franchi, *Molecular beam epitaxy: fundamentals, historical background and future prospects*, Elsevier, 2013.

[36] M. Pohlt, *Exzitonen in gekoppelten 2d Elektronen- und 2d Lochgasen*, PhD thesis, Universität Stuttgart, 2001.

[37] S. Birner et al., IEEE Transactions on Electron Devices **54**, 2137 (2007).

[38] B. Skinner and B. I. Shklovskii, Phys. Rev. B **82**, 155111 (2010).

[39] L. Li et al., Science **332**, 825 (2011).

[40] B. Skinner, Physical Review B **93**, 085436 (2016).

List of Figures

List of Tables

Acknowledgements

During my PhD, I had the support of many people. Some helped me advance in my studies through discussions and advice, others helped me keep my spirits up through leisure activities. I would like to give all of you my sincere thanks.

- **Werner Wegscheider** for giving me the opportunity to conduct the PhD in your research group. Thank you for the trust and freedom you gave me to pursue my project, as well as for great advices and discussion when the project seemed stuck.
- **Werner Dietsche** for the great help and support you gave me during my PhD. Your assistance in analysing of the experimental results and our fruitful discussion were of great importance for the progress of this thesis.
- **Christian Reichl** for the growth of the excellent wafers used in this work and your help operating the cryostats.
- **Mirko Lupatini** for your help and discussions about my research and about your food truck. It was a pleasant time sharing the office with you.
- **Jan Scharnetky** for the introduction to processing in the clean room and help in the interpretation of experimental results. Furthermore, I would like to thank you for all the activities outside of research, especially for introducing me to sailing.
- **Elcin Külah** for the growth of the wafers at the beginning of my PhD. I also enjoyed chatting with you, even though the talks were sometimes rather off-topic.
- **Oded Zilberberg, Andisheh Khedri and Antonio Štrkalj** for the fruitful discussions about my research, and a special thanks to **Oded Zilberberg** for being my co-examiner.
- **Advanced Semiconductor Quantum Material Group** for all the support I received from you and the scientific discussions, which helped me a lot. I had a great time working with you.
- **Sandra Lüdi and Claudia Vinzenz** for the excellent administrative support.

- **My family** for always having my back. You helped me to become the person I am today. I would like to thank all of you for the encouragements I received and the distractions when I needed them. I would like to give a special thanks to my parents **Judith** and **Urs Parolo**. Ich kann gar nicht aufzählen für wie viele Dinge ich euch dankbar bin. Ihr habt mich in jeder Lebenslage unterstützt und mich auch in den Hintern getreten wenn ich es mal wieder brauchte. Danke dass Ihr immer für mich da wart. Ich han eu fest gern.
- **Jasmin Gubler** for being there for me. You always tried to cheer me up when my spirits were low, even though I made it quite tricky sometimes.
- **My friends** for making my time outside of work most pleasing.

This thesis is financially supported by the Swiss National Science Foundation (SNSF) via the NCCR QSIT (National Competence Center in Research – Quantum Science and Technology).

Curriculum Vitae

CURRICULUM VITAE

Name	**Simon Parolo**
Residential Address	Mettenfeld 1 5642 Mühlau
Mobile	078 738 81 69
E-Mail	simon@parolo-gmbh.ch
Nationality	Swiss
Birthday	27. April 1990

Education

January 2017- Present

Eidgenössisch Technische Hochschule Zürich (ETHZ)
Doctoral studies in physics
Research topic: Electron-hole bilayer systems

February 2015 - September 2016

Eidgenössisch Technische Hochschule Zürich (ETHZ)
Master of Science in Interdisciplinary Science
Specialisation: Physics and physical chemistry
Master thesis: Spin-flip tunnelling in an isolated two electron double quantum dot

September 2010 - January 2015

Eidgenössisch Technische Hochschule Zürich (ETHZ)
Bachelor of Science in Interdisciplinary Science
Subject: Physical-Chemical direction
Bachelor thesis: Beryllium Enrichment at the Surface by performing Heat Treatments with a Cu-Be Alloy and Depth Profiling using the ERDA Technique for Applications in UCN-Physics

2006 - 2010

Kantonsschule Wohlen
Major subject: Economy and law
Supplementary subject: Informatics

2002 - 2006

Bezirksschule Muri
Bezirksschulabschluss

Work experience

January 2017 - Present

Department of Physics at ETHZ (Scientific assistance)

- Independent planning and implementation of scientific experiments
- Collection and analysis of measurement data and their interpretation
- Writing of scientific papers
- Attending international conferences, on site and online
- Planning and teaching of exercise classes, following a lecture schedule
- Preparation of semester examinations as well as their supervision and correction
- Supervision and training of new doctoral students

October 2015 - March 2016

ABB Switzerland Ltd Semiconductors (Internship at BiMOS Test & Metrology)

- Support of the production line of silicon wafers
- Support of the development of a new measurement for quality control
- Automation of optical inspection for contamination of wafers

February 2014- June 2015

Department of chemistry at ETHZ (Teaching assistant)

- Teaching assistant for the lecture, Physical chemistry III:
    - Teaching of exercise classes
    - Correction of assignments
- Teaching assistant in the laboratory for physical chemistry
    - Supervising and instructing students in UV/Vis spectrophotometry experiments

January 2010 - June 2014

Avenir Lerncenter (Privat tutor)
- Planning and teaching of private tuition
- Level: High school (age 12-18)

Languages

Native language

(Swiss-) German

Other languages

English
Very good

French
Basic knowledge

Italian
Basic knowledge

Skills

Data processing
Experience with the software Matlab, R-Studios and Origin in order to use them to calculate material properties out of raw/measured data, statistical evaluation and their graphical presentation.

IT-Experience
Coding of simulation using the program NEXTNANO, as well as basic knowledge of Python and Ruby.

Laboratory experience
Processing of semiconductor devices (GaAs/AlAs) in a cleanroom environment using optical lithography, deposition of thin metallic layer and chemical treatment. Characterisation of processed samples with different cryostats (temperature ranging from 4K down to 25mK) by means of direct and alternating voltage as well as external magnetic fields (up to 12T). Experiences in chemistry gained through synthesis of various molecules and their analysis.

Extracurricular Activities

September 2014 - Present

Akademischer Sportverband Zürich (Handball Trainer)
Coach of regular training and leading a beginners course Handball. Planning and implementation of trainings, internal and international tournaments. OC member of an international handball tournament in Zurich.

September 2021

ETH Sustainability Summer School
Participation in the ETH summer school on the topic “Rethinking Waste – Sustainable Solid Waste Management”, which was caried out together with KNUST in Ghana. Identification of a problem as a team and its solution as a team within a Design Thinking Process.

Hobbies

- Sailing
- Scuba diving
- Travelling
- Cooking with friends
- Reading
- Gardening (exotic plants)

References

On request

Appendix

Appendix A: Declaration of personal contribution

In this part I mention the personal contribution of the author, Simon Parolo, to each chapter.

Chapter 1&2: Introduction & Theory

Chapter 1 gives an introduction to the work done in the thesis. It is a collection of already published research. Chapter 2 reviews the physical theories which were used in this thesis. The authors contribution, to these two chapter were the collection and summary of the sources cited in the text.

Chapter 3: Experimental Setups and Measurement Method

The part about MBE is a summary of the cited sources in the text. The improvement of the sample heterostructure started with an idea of Dr. Werner Dietsche. Afterwards, it was developed in various discussion and growth runs. The people which participated in the discussion are:

- Prof. Dr. Werner Wegscheider
- Prof. Dr. Werner Dietsche
- Dr. Christian Reichl
- Dr. Stefan Fält
- Dr. Elcin Külah
- Dr. Matthias Berl
- Simon Parolo

The first wafers used for this work were grown by Dr. M. Berl (no measurements in this thesis). He was in the beginning very much involved in creating the growth recipe. After he finished his PhD, Dr. E. Külah continued growing the wafers. The measurements on samples with a 20 nm thick barrier were grown by her. All other wafers, i.e. the 10 and 15 nm thick barrier, were grown by Dr. C. Reichl.

The clean room fabrication recipe, was developed by the author. It started with an already existing recipe from Dr. Jan Scharnetzky, which was improved with the help of Dr. Mirko Lupatini. Clean room processing of the samples was done by the author.

The measurement setup was developed with the help of Peter Märki, who also provided the author with additional equipment (Voltage adder and IV-converter). The cryostats were already existing in the research group.

Chapter 4, 5 & 6: Results from Various Samples

The electro luminescence measurement was done by Dr. Mirko Lupatini. All other measurements were done by the author as well as the analysis of the experimental data. The theory in section 5.2.1 was developed in discussions with:

- Prof. Dr. Werner Wegscheider
- Prof. Dr. Werner Dietsche

- Dr. Mirko Lupatini
- Simon Parolo

Furthermore, the simulations for this thesis were coded and analysed by Simon Parolo.

Chapter 7: Conclusion and Outlook

The summary of the thesis was done by the author.

Appendix B: Wafer Numbers

List of the wafers used for this thesis

Barrier width	QW Structure	QW Width	Wafer number
20 nm	Zero QW	60 nm	F180622A
20 nm	Double QW	60 nm	F180626B
15 nm	Single QW	120 nm	D190802B
15 nm	Double QW	90 nm	D190802A
10 nm	Single QW	60 nm	D201027B
10 nm	Single QW	90 nm	D201027A
10 nm	Single QW	120 nm	D191010B
10 nm	Single QW	150 nm	D201030A
10 nm	Double QW	60 nm	D201028B
10 nm	Double QW	90 nm	D191010C
10 nm	Double QW	120 nm	D201028A
10 nm	Zero QW	120 nm	D201126C

List of the wafers used in this thesis

Appendix C: Clean Room Procedure

This is a detail description of the fabrication process which was done in the clean room. Samples of approx. 4 × 4 mm were cleaved from the wafer. The processing was done with these samples

Step 1 Defining the mesa

- Clean in acetone 5 min, then IPA 5 min, rinse with DI-water
- Blow dry with N_2
- Dehydration bake on hotplate at 110 °C for 60 s
- Mounting on spinner plate
- Resist AZ1505 (first drop is discarded in the spinner bowl, second drop is put on the sample)
- Spin sample, ramp up in 4 s to 4000 rpm, spin for 45 s at 4000 rpm
- Bake on hotplate at 100 °C for 15 s
- Exposure for 10 s with $10\,\mathrm{mW\,cm^{-2}}$ at 405 nm (Karl Süss mask aligner MJB3)
- Developing in MIF726 for 6 s, rinse with DI-water for 60 s
- Blow dry with N_2
- Visual inspection under optical microscope

Step 2 Etching the mesa

- Prepare etch solution 400 mL H_2O, 8 mL H_2O_2, 2 mL H_2SO_4 (sulfuric acid), stir with magnet bar at 220 rpm
- Determine etch rate with a dummy sample, should be $\approx 2\,\mathrm{nm\,s^{-1}}$
- Etch sample down to target depth
- Stop etching by rinsing the sample with DI-water
- Strip resist in acetone, IPA and rinse with DI-water
- Measure etch depth and adjust etch rate for next samples

Step 3 Patterning n-contacts

- Clean in acetone 5 min, then IPA 5 min, rinse with DI-water
- Blow dry with N_2
- Dehydration bake on hotplate at 110 °C for 60 s
- Mounting on spinner plate
- Resist AZ2020 (first drop is discarded in the spinner bowl, second drop is put on the sample)
- Spin sample, ramp up in 3 s to 3000 rpm, spin for 3 s at 3000 rpm, ramp up in 5 s to 4000 rpm, spin for 45 s at 4000 rpm
- Bake on hotplate at 110 °C for 60 s
- Exposure for 14 s with $10\,\mathrm{mW\,cm^{-2}}$ at 405 nm (Karl Süss mask aligner MJB3)
- Post bake at 110 °C for 60 s
- Developing in MIF826 for 35 s, rinse with DI-water for 60 s

- Blow dry with N_2
- Visual inspection under optical microscope

Step 4 Depostion and annealing of n-contacts

- HCl dip for 5 s to remove surface oxide
- Rinse in DI-water
- Blow dry with N_2
- Mount to metal deposition machine (PLASSYS II) as quickly as possible
- Ar-sputtering for 30 s to remove surface oxide
- Evaporation of contact metal (Ge/ Au/ Ge/ Au/ Ni/ Au) (52.8 nm/ 107.2 nm/ 52.8 nm/ 107.2 nm/ 80 nm/ 100 nm) deposition time (without mounting or pumping) $\approx$ 80 min
- Lift-off in warm (50 °C) acetone for 60 min
- Visual inspection under optical microscope, sample has to remain in acetone or IPA
- Clean with IPA and rinse with DI-water
- Annealing at 470 °C for 5 min (Rapid Thermal Processor (RTA) AS-One 100)

Step 5 Patterning p-contacts

- Clean in acetone 5 min, then IPA 5 min, rinse with DI-water
- Blow dry with N_2
- Dehydration bake on hotplate at 110 °C for 60 s
- Mounting on spinner plate
- Resist AZ2020 (first drop is discarded in the spinner bowl, second drop is put on the sample)
- Spin sample, ramp up in 3 s to 3000 rpm, spin for 3 s at 3000 rpm, ramp up in 5 s to 4000 rpm, spin for 45 s at 4000 rpm
- Bake on hotplate at 110 °C for 60 s
- Exposure for 14 s with 10 mW cm^{-2} at 405 nm (Karl Süss mask aligner MJB3)
- Post bake at 110 °C for 60 s
- Developing in MIF826 for 35 s, rinse with DI-water for 60 s
- Blow dry with N_2
- Visual inspection under optical microscope

Step 6 Deposition and annealing of p-contacts

- HCl dip for 5 s to remove surface oxide
- Rinse in DI-water
- Blow dry with N_2
- Mount to metal deposition machine (PLASSYS II) as quickly as possible
- Ar-sputtering for 30 s to remove surface oxide

- Evaporation of contact metal (Pt/ Ti/ Pt/ Au) (15 nm/ 10 nm/ 15 nm/ 60 nm) deposition time (without mounting or pumping) ≈ 30 min
- Lift-off in warm (50 °C) acetone for 60 min
- Visual inspection under optical microscope, sample has to remain in acetone or IPA
- Clean with IPA and rinse with DI-water
- Annealing at 300 °C for 30 s (Rapid Thermal Processor (RTA) AS-One 100)

Step 7 Bonding

- Glue sample to chip carrier using PMMA in Anisol 1:1
- Wire bonding with Al-bonder (Westbond 7476E), buffer 6
- Bonding of n-contacts, e.g Power:285 Time:60
- Bonding of p-contacts, starting point Power: 100 Time: 200

The bonding of the p-contacts is critical since the p-i-n device is directly below. Therefore, as little power as possible has to be used, to not damage the device. If the bond does not stick, it is suggested to increase bonding time, rather than power.

Appendix D: Photo lithography Mask

Images of the lithography masks used in this thesis.

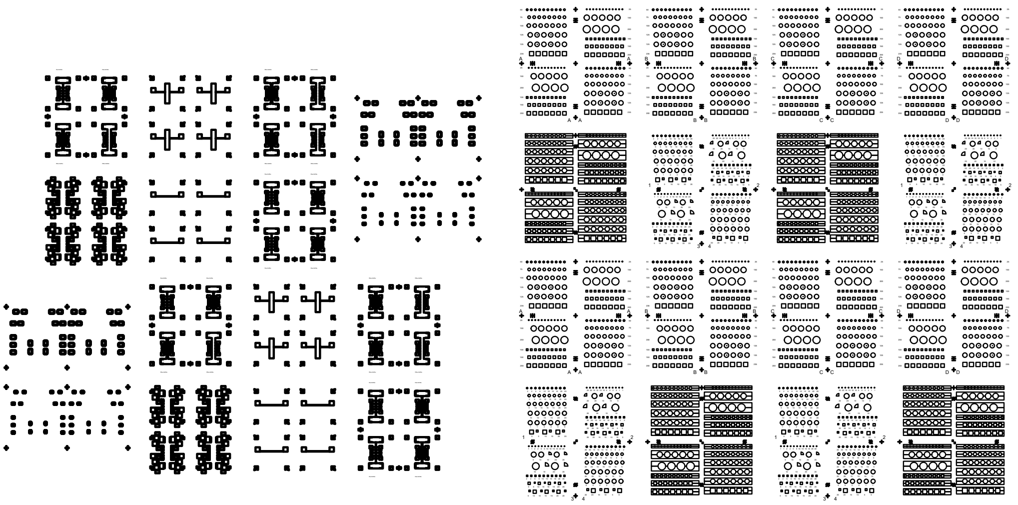

Only the rectangular shaped structures on the top right and bottom left were used for the device fabrication. The bigger rectangles were used for both, mesa and n-contacts, whereas the small ones were used for the p-contacts.

Mask for the fabrication of many p-i-n devices. Each line of the mesa had its specific size. The whole line of mesas is surrounded by the n-contact. The p-contact was drawn either covering the full mesa or only a part of it.

Masks for lithography.

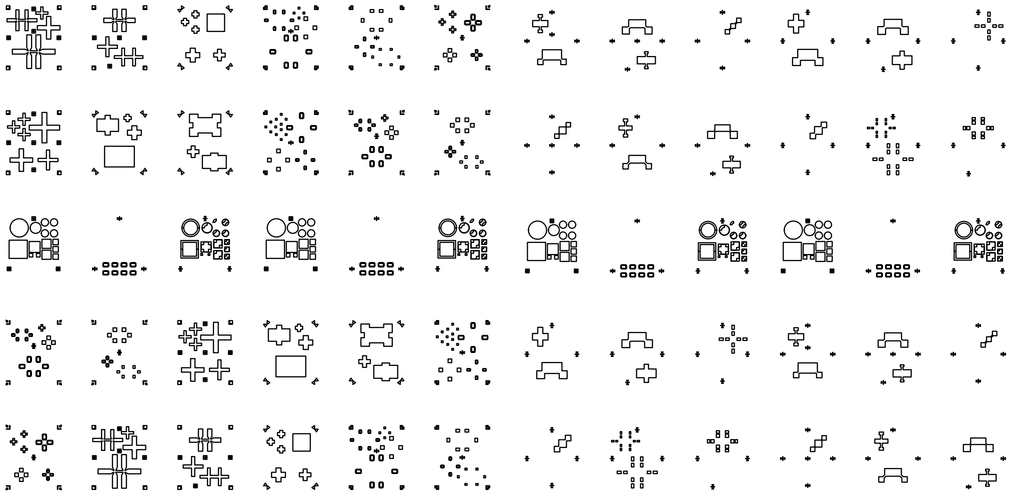

Mask for Mesa and ohmics. The structure was adjusted to allow capacitance measurements and to fabricate separate contacts to each layer. The middle row is dedicated for structures, that allows optical measurements

Mask for isolation and topgates of the mask shown on the left. In order to equip the device with a gate, an insulating layer needs to be fabricated first. The middle row is again for optical devices.

Masks for lithography.

Appendix E: Nextnano Simulation Code

This code was used in the simulations. The simulated structure is a single quantum well with a 10 nm-barrier and a 90 nm wide well

```
#Begin nextnanomat parameter section

$Eigenvalues     = 50   #Number of Eigenvalues calculated in Quantum
$Eigenvalues_out = 30   #Number of Eigenvalues in output

# Concentration of p-Doping(DisplayUnit:10^18 cm^-3)

#$conc_p5 = 5.0E18       #Concentration of p-Doping  Step 5
#$conc_p4 = 4.0E18       #Concentration of p-Doping  Step 4
#$conc_p3 = 3.0E18       #Concentration of p-Doping  Step 3
#$conc_p2 = 2.0E18       #Concentration of p-Doping Step 2
#$conc_p1 = 1.0E18       #Concentration of p-Doping  Step 1

$p = 0.5                #share for decreasing doping

$conc_p5 = 5.0E18        #Concentration of p-Doping  Step 5
$conc_p4 = $conc_p5*$p   #Concentration of p-Doping  Step 4
$conc_p3 = $conc_p4*$p   #Concentration of p-Doping  Step 3
$conc_p2 = $conc_p3*$p   #Concentration of p-Doping  Step 2
$conc_p1 = $conc_p2*$p   #Concentration of p-Doping  Step 1

$conc_n5 = 5E18       #Concentration of n-Doping  Step 5
$conc_n4 = 4E18       #Concentration of n-Doping  Step 4
$conc_n3 = 3E18       #Concentration of n-Doping  Step 3
$conc_n2 = 2E18       #Concentration of n-Doping  Step 2
$conc_n1 = 1E18       #Concentration of n-Doping  Step 1

$alloy_p  = 0.24      #Al-content in p-doping
$alloy_s    = 0.24      #Al-content in spacer
$alloy_b    = 0.8       #Al-content in barrier
#$alloy_n    = 0.0      #Al-content in n-doping

$Temperature = 4.0     #Kelvin

$contacts_p  = 10       #Size of contact region in p-side
$Doping_p    = 100      #Size of p-doping region
$Spacer_p    = 30       #Size of spacer on p-side
$QW_p        = 90       #Size of QW on p-side
$barrier   = 5        #Half of barrier width
$QW_n     = 90       #Size of QW on n-side
#$Spacer_n    = 0        #Size of spacer on n-side
```

```
$Doping_n    = 100      #Size of n-doping region
$contacts_n  = 10       #Size of contact region in n-side

$Doping_Step_p = 20     #Size of doping steps in p, 5 steps @ x nm
$Doping_Step_n = 30     #Size of doping steps in n, 5 steps @ nm

$bias_p_mv   = 1300    #voltage to p contact, change for bias sweep
$bias_p      = $bias_p_mv /1000
$bias_n   = 0      #voltage to n contact has to be negative

$B_p     = $barrier
$Q_p     = $B_p + $QW_p
$S_p     = $Q_p + $Spacer_p
$D1_p    = $S_p + $Doping_Step_p
$D2_p    = $D1_p + $Doping_Step_p
$D3_p    = $D2_p + $Doping_Step_p
$D4_p    = $D3_p + $Doping_Step_p
$D5_p    = $D4_p + $Doping_Step_p
$all_p   = $D5_p + $contacts_p

$B_n     = $barrier
$Q_n     = $B_n + $QW_n
#$S_n     = $Q_n + $Spacer_n
$D1_n    = $Q_n + $Doping_Step_n
$D2_n    = $D1_n + $Doping_Step_n
$D3_n    = $D2_n + $Doping_Step_n
$D4_n    = $D3_n + $Doping_Step_n
$D5_n    = $D4_n + $Doping_Step_n
$all_n   = $D5_n + $contacts_n

$QR_p    = $Q_p + 10
$QR_n    = $Q_n - 10


global{
   simulate1D{}
    # Simulation coordinate system rotated from z to x
   #database = "../Syntax/database_nnp.in"

   # WARNING: check conversion limitations:
   # - only one "simulation-dimension" subsection in
    $numeric-control allowed
   # - only one quantum cluster supported, which must be rectangular
   # - only one quantum model allowed
   # - only one current cluster supported, covering the
```

```
    whole simulation area

   crystal_zb{
      x_hkl = [1, 0, 0]
      y_hkl = [0, 1, 0]
   }

   substrate{
      name = "GaAs"
   }

   temperature = $Temperature

}

grid{
   xgrid{
      line{ pos = -$all_p spacing = 0.25 }
      line{ pos = -$S_p spacing = 0.25 } # inserted
      line{ pos = $Q_n spacing = 0.25 }
      # spacing changes from 0.25 to 0.5
      line{ pos = $all_n spacing = 0.25 }
      }
}


structure{
   output_alloy_composition{}
   output_impurities{}
   #output_generation{}
   #output_contact_index{}

   region{
      line{x=[-$all_p,-$B_p]}
      binary { name = "GaAs"  }
      contact{ name = "dummy_p" }
   }
   region{
      line{x=[$B_n,$all_n]}
      binary { name = "GaAs"  }
      contact{ name = "dummy_n" }
   }
   region{
      everywhere{}
      binary{ name = "GaAs" }
```

```
}

region{
   line{
      x = [-$D5_p, -$S_p]
   }
   ternary_constant{
      name = "Al(x)Ga(1-x)As"
      alloy_x = $alloy_p
   }
}
region{
   line{
      x = [-$S_p, -$Q_p]
   }
   ternary_constant{
      name = "Al(x)Ga(1-x)As"
      alloy_x = $alloy_s
   }
}
region{
   line{
      x = [-$Q_p, -$B_p]
   }
   binary{
      name = "GaAs"
      # AlGaAs barriers, alloy concentrations specified below
   }
}
region{
   line{
      x = [-$B_p, $B_n]
   }
   ternary_constant{
      name = "Al(x)Ga(1-x)As"
      alloy_x = $alloy_b
   }
}
region{
   line{
      x = [$B_n, $Q_n]
   }
   binary{
      name = "GaAs"
   }
```

```
   }
#   region{
#      line{
#         x = [$Q_n, $S_n]
#      }
#      ternary_constant{
#         name = "Al(x)Ga(1-x)As"
#         alloy_x = $alloy_s
#      }
#   }
   region{
      line{
         x = [$Q_n, $D5_n]
      }
      binary{
         name = "GaAs"
      }
   }
   region{ #contact p
      line{
         x = [-$all_p, -$D5_p]
      }
      contact { name = contact_p }
      ternary_constant{
         name = "Al(x)Ga(1-x)As"
         alloy_x = $alloy_p
      }
   }
   region{ #contact n
      line{
         x = [$D5_n, $all_n]
      }
      contact { name = contact_n }
      binary{
         name = "GaAs"
      }
   }
   region{ # doping acceptors
      line{
         x = [-$D5_p,-$D4_p] # [nm]
      }
      doping{
         constant{
            name = "p_doping"
# properties of this impurity type have to be specified below
```

```
            conc = $conc_p5
# acceptor concentration (DisplayUnit:10^18 cm^-3)
         }
      }
   }
   region{ # doping acceptors
      line{
         x = [-$D4_p,-$D3_p] # [nm]
      }
      doping{
         constant{
            name = "p_doping"
# properties of this impurity type have to be specified below
            conc = $conc_p4
 # acceptor concentration (DisplayUnit:10^18 cm^-3)
         }
      }
   }
   region{ # doping acceptors
      line{
         x = [-$D3_p,-$D2_p] # [nm]
      }
      doping{
         constant{
            name = "p_doping"
            conc = $conc_p3
         }
      }
   }
   region{ # doping acceptors
      line{
         x = [-$D2_p,-$D1_p] # [nm]
      }
      doping{
         constant{
            name = "p_doping"
            conc = $conc_p2
         }
      }
   }
   region{ # doping acceptors
      line{
         x = [-$D1_p,-$S_p] # [nm]
      }
      doping{
```

```
      constant{
         name = "p_doping"
         conc = $conc_p1

      }
   }
}
region{ # doping donor
   line{
      x = [$D5_n,$D4_n] # [nm]
   }
   doping{
      constant{
         name = "n_doping"
         conc = $conc_n5
      }
   }
}
region{ # doping donor
   line{
      x = [$D4_n,$D3_n] # [nm]
   }
   doping{
      constant{
         name = "n_doping"
         conc = $conc_n4
      }
   }
}
region{ # doping donor
   line{
      x = [$D3_n,$D2_n] # [nm]
   }
   doping{
      constant{
         name = "n_doping"
         conc = $conc_n3
      }
   }
}
region{ # doping donor
   line{
      x = [$D2_n,$D1_n] # [nm]
   }
   doping{
```

```
         constant{
            name = "n_doping"
            conc = $conc_n2
         }
      }
   }
   region{ # doping donor
      line{
         x = [$D1_n,$Q_n] # [nm]
      }
      doping{
         constant{
            name = "n_doping"
            conc = $conc_n1
         }
      }
   }
}

impurities{
   acceptor{ # n-type, p-type
      name = "p_doping"
      energy = -1000#0.027 # p-C-in-GaAs
      degeneracy = 4
# degeneracy of energy levels, 2 for n-type, 4 for p-type
   }
   donor{ # n-type, p-type
      name = "n_doping"
      energy = -1000 #0.0058 # n-Si-in-GaAs
      degeneracy = 2
 # degeneracy of energy levels, 2 for n-type, 4 for p-type
   }
}

classical{ # Check if Delta{} or X{} is needed
   Gamma{}
   L{}
   X{}
   HH{}
   LH{}
   SO{}
   output_bandedges{ averaged = no }
   output_bandgap{}
   output_carrier_densities{}
   output_ionized_dopant_densities{}
```

```
   output_intrinsic_density{}
}


poisson{
   output_potential{}
   output_electric_field{}
}


contacts{
      fermi{ name = "dummy_p" bias = $bias_p  }
# only needed to define reference energy
      fermi{ name = "dummy_n" bias = $bias_n }
   ohmic{
      name = contact_p
      bias = $bias_p
#apply voltage to poisson-cluster (required for Dirichlet)
   }
   ohmic{
      name = contact_n
      bias = $bias_n
   }

   #fermi{ name = "dummy" bias = 0} # define reference energy
}

currents{
   mobility_model = constant
   recombination_model{
      radiative = yes
      SRH        = yes    # 'yes' or 'no'
      Auger      = yes    # 'yes' or 'no'
   }
   output_fermi_levels{}
   output_mobilities{}
   output_recombination{}
   output_currents{}
}




quantum {
   region{
```

```
      name = "QR_p"
      x = [-$QR_p, -1]
      boundary{
         x = dirichlet
#Dirichlet boundary condition for the Schroedingerequation psi=0
       #  x = neumann
#Neumann boundary condition for the Schroedinger eq, dpsi/dx = 0
      }

      Gamma{
         num_ev = $Eigenvalues
  # 100 eigenvalues have to be calculated
      }
      HH{
         num_ev = $Eigenvalues
         # 100 eigenvalues have to be calculated
      }

      LH{
         num_ev = $Eigenvalues
         # 100 eigenvalues have to be calculated
      }

      SO{
         num_ev = $Eigenvalues
         # 100 eigenvalues have to be calculated
      }

      output_wavefunctions{
         max_num = $Eigenvalues_out
 # only 20 eigenfunctions from 100 calculated are shown in output
         amplitudes = no
         probabilities = yes
      }
   }

   region{
      name = "QR_n"
      x = [1, $QR_n]
      boundary{
         x = dirichlet
       #  x = neumann
      }

      Gamma{
```

```
         num_ev = $Eigenvalues
         # 100 eigenvalues have to be calculated
      }

     # L{
# put to comments, if L band does not contribute to the density
     #    num_ev = 100 # 100 eigenvalues have to be calculated
     # }

     # X{
# put to comments, if X band does not contribute to the density
     #    num_ev = 100 # 100 eigenvalues have to be calculated
     # }

      HH{
         num_ev = $Eigenvalues
         # 100 eigenvalues have to be calculated
      }

      LH{
         num_ev = $Eigenvalues
         # 100 eigenvalues have to be calculated
      }

      SO{
         num_ev = $Eigenvalues
         # 100 eigenvalues have to be calculated
      }

      output_wavefunctions{
         max_num = $Eigenvalues_out
# only 20 eigenfunctions from 100 calculated are shown in output
         amplitudes = no
         probabilities = yes
      }
   }
}


output{
   material_parameters{
   }
}
```

```
run{
  #solve_strain{}             # solves the strain equation
  #solve_poisson{}            # solves the Poisson equation
   solve_current_poisson{}
# solves the coupled current and Poisson eq self-consistently
   solve_quantum{}            # solves the Schroedinger equation
   outer_iteration{}
#solves the Schroedinger, Poisson (and current) eq self-consistently


}

database{
binary_zb {   #
name =   "GaAs"
#  conduction-band-energies   =   2.979e0   3.275e0   3.441e0
# DEFAULT at 0 K # check if you have to change this line for nn+
#  6x6kp-parameters   =   -16.22e0   -3.86e0   -17.58e0
#[nextnano++] # L,M,N [hbar^2/2m] (--> divide by hbar^2/2m)
# check if you have to change this line for nn+
#  0.341e0   # [nextnano++] # delta_(split-off) in [eV]
# check if you have to change this line for nn+
dielectric_consts{
static_a = 12.93e0
   }
valence_bands {
bandoffset =  1.346e0
HH{
mass = 0.510e0
   }
LH{
mass = 0.082e0
   }
SO{
mass = 0.172e0
   }
}
conduction_bands {
Gamma{
bandgap = 1.519e0
bandgap_alpha = 0.5405e-3
bandgap_beta = 204e0
mass = 0.067e0
   }
L{
```

```
bandgap = 1.815e0
bandgap_alpha = 0.605e-3
bandgap_beta = 204e0
mass_l = 1.9e0
mass_t = 0.0754e0
   }
X{
bandgap = 1.981e0
bandgap_alpha = 0.460e-3
bandgap_beta = 204e0
mass_l = 1.3e0
mass_t = 0.23e0
   }
}
   }

}
```